The Impact of Aerosols on the Stratiform Clouds over Southern West Africa: A Large-Eddy Simulation Study

Lambert Delbeke[1], Chien Wang[1], Pierre Tulet[1], Cyrielle Denjean[2], Maurin Zouzoua[3], Nicolas Maury[4] and Adrien Deroubaix[5]

[1]Laboratoire d'Aérologie, Université de Toulouse, CNRS, UT3, IRD, Toulouse, France
[2]CNRM, Université de Toulouse, Météo-France, CNRS, Toulouse, France
[3]Laboratoire Atmosphères, Milieux, Observations Spatiales, IPSL, CNRS, Guyancourt, France
[4]CNRM, Université de Toulouse, Météo-France, CNRS, Toulouse; now at LMD/IPSL, Paris, France
[5]IUP, Institute of Environmental Physics, University of Bremen, Bremen, and Max Plank Institute for Meteorology, Hamburg, Germany

Correspondence to: Chien Wang (chien.wang@aero.obs-mip.fr), Cyrielle Denjean (cyrielle.denjean@meteo.fr)

Abstract. ~~Low~~ The low level stratiform clouds (LLSCs) covering a large area appear frequently during the wet monsoon season in southern West Africa. This region is also ~~the~~ a place where different types of aerosols coexist, including the biomass burning aerosols coming from Central and South Africa and the ~~anthropogenic~~ aerosols emitted by local anthropogenic activities. We investigate the indirect and semi-direct ~~and indirect~~ effects of these aerosols on the ~~diurnal~~ life cycle of LLSCs by ~~constructing~~ conducting a case study based on the airborne and ground-based observations from the field campaign of Dynamic-Aerosol-Chemistry-Cloud-Interaction in West Africa (DACCIWA)~~ field campaign~~. This case is modell~~l~~ed using a Large Eddy Simulation (LES) model with fine ~~scale~~ resolution and in-situ aerosol measurements including size distribution and chemical composition. The model has successfully reproduced the observed life cycle of the LLSC, from stratus formation to stabilization during the night, and to the upward development after sunrise until break-up of cloud deck in the late afternoon. ~~Various~~ Additional sensitivity simulations using different measured aerosol profiles also suggest that aerosols can affect the cloud life cycle through both the indirect and semi-direct effect. ~~Despite precipitation produced by the modeled cloud is nearly negligible, cloud lifetime is still sensitive to the aerosol concentration.~~ As expected, modeled cloud microphysical features including cloud droplet number concentration, mean radius, and thus cloud reflectivity are all controlled by aerosol concentration. However, it is found that the difference in cloud reflectivity is not always the only factor in determining the variation of the incoming solar radiation at ground and cloud life cycle ~~specifically beyond~~ after sunrise. Instead, the difference in ~~cloud-void space~~cloud fraction brought by dry air entrainment from above and thus the speed of consequent evaporation - also influenced by aerosol concentration, is another important factor to consider. Clouds influenced by higher aerosol concentrations and thus having higher number concentration and smaller sizes of cloud droplets are found to evaporate more easily and thus impose a lower cloud fraction.~~Results have shown that clouds in the case with lower aerosol concentration and larger droplet size appear to be less affected by entrainment and convection.~~ In addition, we ~~found~~ find that an excessive atmospheric heating up to 12 $K\ day^{-1}$ produced by absorbing black carbon aerosols (BC) in our modeled cases ~~can also affect the life cycle of modeled clouds. Such a heating is found to~~can lower

the height of cloud top and liquid water path, resulting a ~~less~~ weaker extent in vertical development while a higher cloud fraction, ~~and accelerating~~ delaying intense cloud break-up until later afternoon, making a positive contribution to the indirect effect. ~~The semi-direct effect impacts on indirect effect by reducing cloud reflectivity particularly in case of polluted environment. Finally, semi-direct effect is found to contribute positively to the indirect radiative forcing due to a decreased cloud-void space, and negatively by causing~~While the resulted thinner clouds from such a heating, on the other hand, ~~that~~ would break~~-~~ up faster in late afternoon, ~~all depending on the phase in stratiform cloud diurnal cycle~~thus contributing negatively to the indirect effect.

1. Introduction

Low-level stratiform clouds (LLSCs) have a higher albedo ~~(Hartmann et al., 1992; Chen et al., 2000)~~ and a larger cloud deck covering Earth's surface ~~more~~ than ~~any~~many other types of clouds~~ type~~ (Hartmann *et al*., 1992; Chen *et al*., 2000; Eastman and Warren, 2014). Their reflection of solar radiation is thus ~~are~~ important to Earth's radiative budget. ~~through the reflection of solar radiation due to their high albedo (Hartmann et al., 1992; Chen et al., 2000) and large cloud deck covering Earth's surface more than any other cloud type (Eastman and Warren, 2014).~~ LLSCs often occupy the upper few hundred meters in the planetary boundary layer (PBL), and their persistent appearance relies on a stable PBL that is normally associated with a large-scale subsidence above ~~PBL under~~because of a high-pressure system. ~~LLSCs~~ These clouds are often formed over cooler subtropical and mid-latitude oceans, constantly covering more than 50% of these areas (Wood, 2012). During the West African monsoon season, LLSCs frequently form over continental southern West Africa (SWA) in the night and ~~would likely~~usually break up in the early afternoon of the following day ~~there~~ (Schrage and Fink, 2012; Schuster *et al*., 2013). ~~LLSCs are, under~~ Under a polluted condition~~s~~, LLSCs are characterized by numerous and small cloud droplets, increasing the cloud albedo, suppressing drizzle, and extending the cloud lifetime (Twomey, 1957; Haywood and Boucher, 2000; Liu *et al*., 2014; Carslaw *et al*., 2017). The presence of LLSCs impacts on the radiative budget of ~~atmospheric boundary layer~~the atmosphere, ~~and~~ surface fluxes, ~~and also affect~~ the diurnal cycle of the convective boundary layer, and thus the regional climate (Knippertz *et al*., 2011; Hannak *et al*., 2017). However, the diurnal cycle of LLSCs is still poorly represented in weather and climate models, especially over SWA, because the processes behind the variability of LLSCs cover remain elusive (Knippertz *et al*., 2011; Hannak *et al*., 2017; Hill *et al*., 2018).

Stratiform clouds are sensitive to aerosol ~~properties (~~concentration, chemical composition,~~stry)~~ and vertical distribution. This is because that aerosol can directly scatter or absorb solar radiation (the direct effect or aerosol-radiation effect), or by serving as cloud nuclei, influence cloud microphysical structure and thus reflectance or lifetime (the indirect aerosol effects or radiative effect of aerosol-cloud interaction plus cloud adjustment) (Boucher *et al*., 2013). The heating associated with aerosol absorption of solar radiation would be able to perturb atmospheric thermodynamic stability and thus dynamical processes as well (the semi-direct effect) (Hansen *et al*., 1998). Such a semi-direct effect can be positive or negative depending on the relative distribution of the aerosol with respect to clouds (*e.g*., Johnson *et al*., 2004; Feingold *et al*., 2005). All these effects can modify the energy budget and thus the status of the planetary boundary layer where the stratiform clouds form and evolve. Aerosols inside stratiform clouds ~~are~~ can also be modified by aqueous physi~~c~~o-chemical processes ~~which can influence the aerosol concentration~~

(Wood, 2012). Interactions between aerosols and clouds, and their effects on radiation, precipitation, and regional circulations, remain one of the largest uncertainties in understanding and projecting climate change. Indeed, the indirect effect of aerosol is still difficult to estimate (Boucher *et al*., 2013~~IPCC 2021~~). ~~and c~~Climate models struggle to minimize such uncertainties (Li *et al*., 2022). ~~Some aerosol constituents such as black carbon absorb a substantial amount of shortwave radiation, which results in rapid atmospheric thermodynamic adjustments. This semi-direct aerosol radiative effect can be positive or negative depending on the relative distribution of the aerosol with respect to clouds.~~ Several previous studies were conducted to investigate aerosol-clouds interactions ~~of~~ in LLSCs using high-resolution Large-Eddy Simulation (LES) models, though ~~but~~ mainly on cases over ocean (*e.g.*, Ackerman *et al*., 2004; Sandu *et al*., 2008; Twohy *et al*., 2013; Flossmann and Wobrock, 2019), where surface fluxes ~~are having~~often have insignificant ~~little~~ diurnal variation~~,~~ and latent heat alongside moisture ~~is mainly provided by~~from evaporation ~~from~~ at sea surface ~~to maintain the stratiform cloud layer~~dominate, differing from the ~~. By contrast over~~cases over land~~, moisture supply is dependent on the characteristics of the surface~~ (Wood, 2012; Ghonima *et al*., 2014).

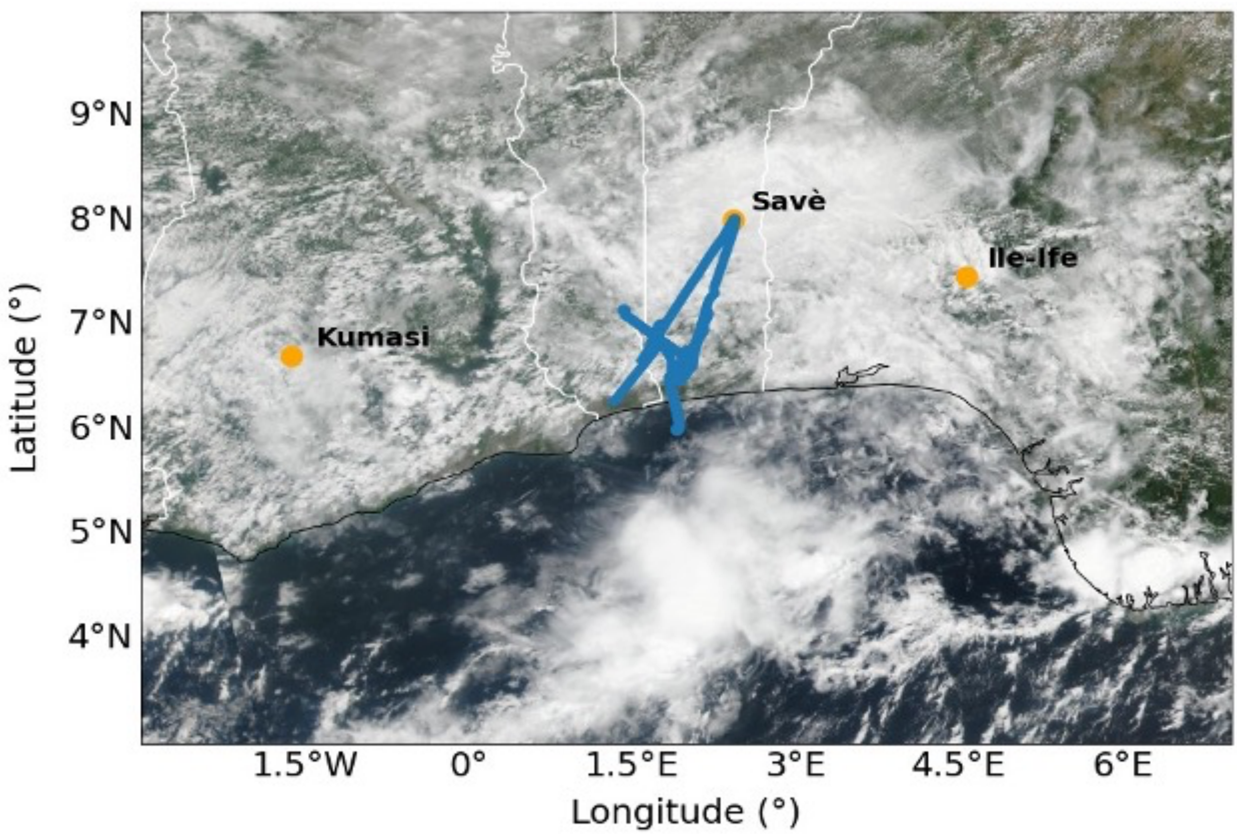

Figure 1. Map of southern West Africa with Savè, Kumasi and Ile-Ife locations and the flight track (blue line) of the ATR-42 the 3 July 2016 with NASA Suomi NPP/VIIRS true color corrected reflectance (https://worldview.earthdata.nasa.gov/).

During the West Africa Monsoon (WAM), aerosols can come from both local and remote sources to SWA. ~~Large~~ A large amount of Biomass Burning Aerosols (BBA) can be~~are~~ transported from southern and Central African towards SWA during the summer monsoon (Haslett *et al*., 2019). These air masses are ~~further~~ also loaded with additional aerosols from anthropogenic emissions upon reaching the highly urbanized regions near the coast (Chatfield *et al*., 1998; Sauvage *et al*., 2005; Mari *et al*., 2008; Murphy *et al*., 2010; Reeves *et al*., 2010; Menut *et al*., 2018; Haslett *et al*., 2019). A significant quantity of wind-blown mineral dust aerosols emitted from the Sahara and Sahel throughout the year with a peak in springtime (Marticorena and Bergametti, 1996) can also reach SWA, ~~far south~~ often in June (Knippertz *et al*., 2017). Local sources of aerosols in SWA are related to anthropogenic activities near the coast, from where polluted plumes would transport inland (Deroubaix *et al.*, 2019). These emissions are ~~supposed~~ projected to increase with the expected growth of the population (Liousse *et al*., 2014). ~~These d~~Different emission sources ~~of aerosols give~~also lead to a complex mix of ~~species~~ aerosol constituents ~~with a high loading~~in the aera, having a serious impact on human health (Bauer *et al*., 2019)~~, and also~~and possibly complicating the aerosol impacts on the diurnal cycle of LLSCs as well as precipitation over SWA (Taylor *et al*., 2019).

The DACCIWA project was designed to better characterize cloud-aerosol-precipitation interactions in SWA (Knippertz *et al*., 2015). The measurement campaign conducted in June-July 2016 has provide~~ds~~d a comprehensive set of ground-based and airborne measurements of clouds and aerosols ~~in June-July 2016~~ (Knippertz *et al*., 2017; Kalthoff *et al*., 2018; Flamant *et al*., 2018) and inspired model analyses. ~~Measurements~~ The measurements were conducted at three supersites, Savè (Benin), Kumasi (Ghana) and Ile-Ife (Nigeria) (Fig.1) and coordinated with three research aircrafts: the French ATR-42 operated by SAFIRE (Service des Avions Français Instrumentés pour la Recherche en Environnement), the British Twin Otter operated by British Antarctic Survey, and the German Falcon aircraft operated by DLR (Deutsches Zentrum für Luft und Raumfahrt). Additional radiosoundings were launched from Savè with high temporal frequency, which specifically benefits the monitoring of the LLSCs diurnal evolution.

Based on observations and a parcel model~~ing~~, Taylor *et al.* (2019) and Denjean *et al*. (2020a) showed that ~~the majority of~~most cloud condensation nuclei and absorbing aerosols observed during DACCIWA campaign were from ubiquitous long-range transported BBA, causing a polluted background which limits the effect of local pollution on cloud properties and aerosol radiative effects. ~~Modeling studies have suggested that light-absorbing aerosols from combustion sources like BBA and anthropogenic sources can impact on the formation, evolution, and precipitation of LLSCs, especially over south-eastern Atlantic.~~ Using COSMO-ART model in a simulation for 2-3 July 2016 case, Deetz *et al*. (2018) found that under the influence of the Maritime Inflow (MI, cold air) from Guinean Gulf, stratus-stratocumulus transition is susceptible to the aerosol direct effect, resulting in a spatial shift in the MI front and a temporal shift of the cloud transition. Over SWA and influenced by anthropogenic emission sources, the break-up time of LLSCs can be delayed by one hour and daily precipitation rate can decrease by 7.5% according to Deroubaix *et al*. (2022). Moreover, the semi-direct and indirect effects of aerosol were also studied together by varying respective magnitude or emissions of anthropogenic aerosols, ~~but they were~~though not being examined separately. Haslett *et al*. (2019) ~~denote~~ indicated that cloud droplets number concentration could increase~~s~~ up to 27 % due to transported BBA using COSMO-ART, making cloud and rain less sensitive to ~~future~~ further increase in regional anthropogenic emissions~~ on regional scale~~.

The impact of sedimentation on LLSCs has been studied by Dearden *et al*. (2018) using the Met Office NERC Cloud model (MONC) who ~~highlight~~ demonstrated that sedimentation of cloud droplets, determined by droplet size, could affect liquid water path by removing droplets from the entrainment zone, or by lowering the cloud base and creating more heterogeneous cloud structure. Menut *et al*. (2019) showed with W~~F~~RF-CHIMERE that a decrease of anthropogenic emissions along the SWA coast led to a northward shift of the monsoonal precipitation and the increase of surface wind speed over arid region in the Sahel, resulting in an increase of mineral dust emission. These previous modeling studies all highlighted in a regional scale ~~and~~ while considering only ~~certain~~ limited aerosol chemical compositions~~, however, they did not~~ rather than ~~take into account~~ all aerosol species particularly black carbon (BC) ~~detected~~ measured during the field campaign ~~especially black carbon (BC)~~. Pedruzo-Bagazgoitia *et al*. (2020) analyzed the stratocumulus-cumulus transition at a fine scale (a dozen of kilometer sidelong) using a LES at high resolution (50x50 m^2), though ~~but without considering~~ aerosol~~s~~ effects were not being taken into consideration.

The aim of this study is to understand the ~~relative~~ specific impacts of local and transported aerosols on the life cycle of LLSCs during the monsoon period over SWA. In doing so, ~~by using~~ observational data obtained from the well-documented DACCIWA field campaign have been used to constrain ~~alongside~~ a high-resolution LES model including an interactive aerosol module that is able to represent the complex aerosol compositions. This model~~l~~ing ~~case~~ effort is also among ~~one of~~ a few studies that model and analyze stratiform cloud diurnal cycle over land rather than ocean. ~~For this purpose, using observational data we firstly identified a reference case for modeling, that is a LLSCs case observed on July 3, 2016, at Savè site. The~~ A ~~short~~ description of observations, data, and the model as well as configurations of different simulations will be presented in the Method section after the Introduction. Then ~~an~~ the results of an analysis ~~will be driven~~aiming to understand and validate the modeled reference case ~~compared to~~against measurements will be discussed. ~~Then~~Thereafter, the results from several sensitivity simulations will be presented. These sensitivity simulations use various observed aerosol profiles with different size distributions and chemical compositions, designed to examine the indirect and semi-direct effects of aerosols on the life cycle of modeled LLSCs. This makes the analysis the first such modeling attempt within the framework of DACCIWA campaign. ~~to assess the aerosol effects on stratiform clouds using observed aerosol data, we have constructed several different aerosol profiles which differ in term of aerosol size distribution and chemistry for sensitivity modeling studies. A first sensitivity analysis will be driven to assess the impact of aerosol concentration and consequently the indirect effect on LLSC diurnal cycle. Another analysis will be focused on the impact of aerosol optical properties by switching off aerosol (semi) direct contributions to the radiative budget to exhibit the relative changes imposed by direct and semi-direct effects. In the DACCIWA framework, such analysis is a first and differs from other modelling studies by performing this set of scenarios and configurations in order to better investigate on indirect and semi-direct effects of aerosols from biomass burning and local anthropogenic sources. Finally, this study will conclude by~~The last section of the paper will summarize ~~a summary of~~major research findings of this study.

2. Methods

2.1 Observational data~~s~~

~~The relevant~~We have used certain measurements of the DACCIWA field campaign ~~used~~ to select our LLSC case and to configure the model simulations. These data are described as follows.~~:~~

i) Radiosonde data~~s~~: During DACCIWA campaign, radiosondes were launched with the MODEM system every 1 to 1.5 hour between 17:00 and 11:00 UTC (the local time of Benin is UTC+1) at the supersite of Savè in Benin ~~(local time of Benin is UTC+1)~~. This site is located ~~at~~ 185 km from the coast and 166 m above sea level. ~~where t~~The area is rather flat, and the vegetation is mainly composed of small trees and shrubs. Temperature, pressure, relative humidity, and wind vertical profiles ~~in the lower atmosphere (up to~~below 1500 m above ground level were measured with a 1s temporal ~~resolution~~ interval (4 - 5m of vertical resolution) (Derrien *et al*., 2016). These sondes were obtained using~~e~~ two balloons of different volumes to reach a preset time of ascent, and after the cutting of the larger balloon, the second one would be used ~~allows~~ to retrieve the sonde for another use (Legain *et al*., 2013).

ii) Ground-based measurements: At the supersite of Savè, ~~meteorological parameters were measured using different instruments. A~~a CHM15k Ceilometer was deployed by the Karlsruher Institut für Technologie (KIT) to measure the cloud base height continuously with a 1 min ~~resolution~~ interval and a 15 m vertical resolution,~~. Three cloud base heights are recorded~~ based on ~~from~~ the backscatter profiles produced by the lidar with a wavelength of 1064 nm and a 5-7 kHz rate (Handwerker *et al*., 2016). The cloud cover was monitored every day by using a MOBOTIX S15 cloud camera, installed by Université Paul Sabatier (UPS) team, to obtain pictures in visible and IR every 2 min. The aperture angles for the IR channel corresponds to a 158 m x 114 m area at a height of 200 m and pictures are coded in RGB components. A microwave radiometer (humidity and temperature profiler HATPRO-G4 from Radiometer Physics GmbH) was installed by KIT to measure brightness temperature to retrieve absolute humidity, liquid water path, and air temperature. The surface heat and radiation fluxes were measured with an energy balance station deployed over grass and bushes. Additional measurements ~~were also~~include soil heat flux, air density, and turbulence parameters ~~as well as sensible and latent heat flux~~.

iii) Airborne measurements: The aircraft campaign took place from 29 June to 16 July 2016~~. It was~~, conducted collaboratively ~~a collaborative work between~~by three research aircraft. ~~but i~~In this study, only ~~the~~ data from the ATR-42 ~~is~~ were used ~~selected~~ as it flew around Savè between 10:00 and 11:00 UTC and probed the cloud layer. The cloud droplet size distribution was measured with a cloud droplet probe (CDP) (Taylor *et al*., 2019). The chemical composition for non-refractive compounds was measured with ~~an~~ the Aerodyne compact Time-of-Flight Aerosol Mass Spectrometer (HR-ToF-AMS) (Brito *et al*., 2018). The black carbon (BC) mass concentration was measured with a single particle soot photometer (SP2) (Denjean *et al*., 2020b). The aerosol ~~number~~ size distribution was measured with a custom-built scanning mobility sizer spectrometer (SMPS, 20–485 nm), an ultra-high sensitivity aerosol spectrometer (UHSAS, 0.04–1 μm), and an optical particle counter (OPC GRIMM model 1.109, 0.3–32 μm) corrected for the complex refractive index provided in Denjean *et al.* (2020a). The total number concentration ~~number~~ of particles larger than 10 nm was measured by a condensation particle counter (CPC, model MARIE). Meteorological variables such as temperature, humidity, pressure, and wind speed and direction were also measured by a suite of airborne instruments. A gas concentration analyzer was used to measure certain chemical gases including CO_2, CH_4, and CO.

2.2 Description of the studied case

Our study analyzes the diurnal cycle of LLSCs based on the observed case ~~study~~ of 3 July 2016 at the Savè supersite (Fig. 2). The cloud deck formed during the night, at around 02:00 UTC, close to the appearance of ~~the core of~~ the core Nocturnal-Low-Level Jet (NLLJ), which could have a maximum speed around 6 m s^{-1} (Kalthoff *et al.*, 2018), ~~-~~associated with a maximum cooling (Lohou *et al.*, 2020). At formation, the cloud base and top heights were located around 310 ± 30 m and 640 ± 100 m, respectively, and were maintained due to the cloud top radiative cooling and cold advection (Dione *et al.*, 2019).

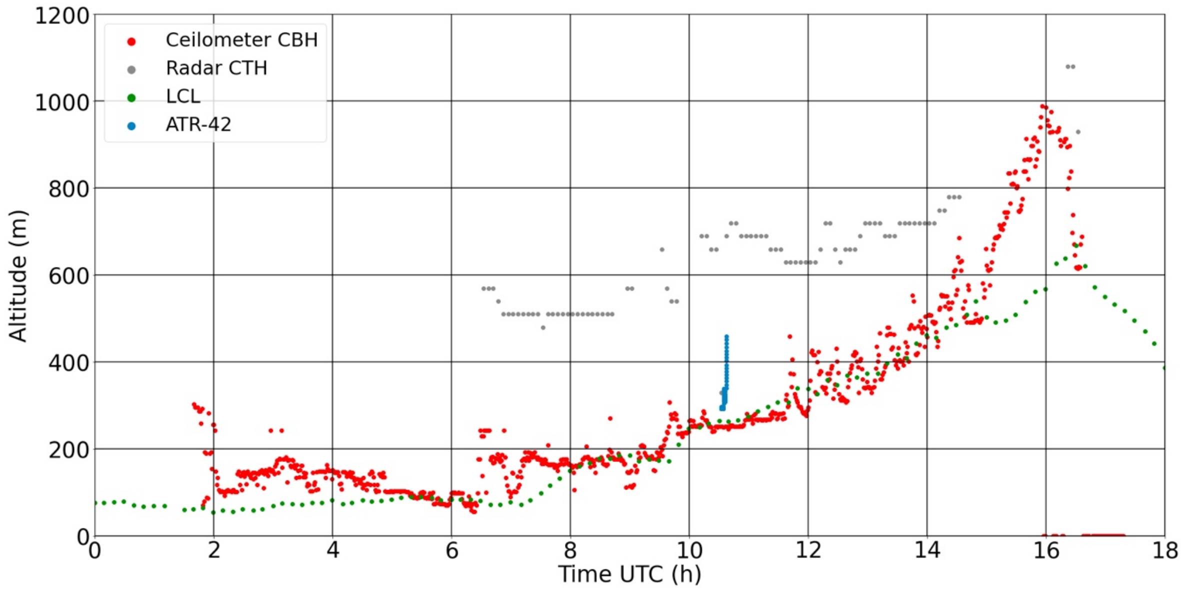

Figure 2. 3 July cloud evolution with the representation of the Cloud Base Height (CBH), the Cloud Top Height (CTH), LCL and ATR-42 flight track near Savè.

The diurnal cycle of LLSCs over SWA typically involves four phases: the stable phase, jet phase, stratus phase, and convective phase (Dione *et al.*, 2019; Lohou *et al.*, 2020). The stable phase begins just after sunset and is characterized by a weak monsoon flow and the cessation of buoyancy-driven turbulence within the PBL, ~~(~~generated by surface heating~~)~~ ~~within the PBL~~ (Zouzoua *et al.*, 2021). The jet phase corresponds to the settlement of key drivers of cooler air advection. Maritime I~~i~~nflow (MI), a cold and slightly humid air mass from the Guinean coast, often reaches Savè at the end of the afternoon (between 16:00 UTC and 20:00 UTC), then is followed by the NLLJ formation ~~occurs~~ (Adler *et al.*, 2019). The stratus phase begins with LLSC formation when ~~the~~ advective cooling continuously increases the relative humidity (RH) until air reaches saturation ~~is reached~~ between 22:00 and 06:00 UTC. Turbulent mixing beneath the NLLJ alongside strong radiative cooling at the cloud top leads to the persistence of a thick stratus layer (Schuster *et al.*, 2013; Babic *et al.*, 2019). The LLSCs life cycle ends during the final convective phase which begins when the PBL develops vertically due to solar heating at the surface alongside a weak radiative cooling at cloud top (*e.g.*, Ghonima *et al.*, 2016). By using dataset from Savè supersite, Zouzoua *et al.* (2021) identified three scenarios of evolution depending on the LLSCs coupling to the surface at sunrise. The coupling was assessed by the departure between the Cloud Base Height (CBH) and the Lifting Condensation Level (LCL).

The LLSCs observed on 3 July 2016 follow the four aforementioned phases and evolve by scenario C described by Zouzoua *et al*. (2021) as seen in Figure 2.~~;~~ The cloud~~the cloud~~ is coupled to the surface at sunrise (06:30 UTC), ~~and~~ its base rises with growing PBL until ~~its~~ break-up occurs in the late afternoon ~~(~~around 16:00 UTC~~)~~. ~~This c~~The cloud deck of July 3 case stands longer (2-3 hours more) compared to other LLSCs observed during the campaign. The co-located Ka band mobile, dual-polarization Doppler radar (8.5 mm, 35.5 MHz) ~~radar~~ at Savè supersite ~~allows the detection of~~detected light drizzle precipitation from higher clouds in a rather short period during the first hours of the convective phase, while no precipitation was detected by the surface rain gauge. Thus, this late LLSC break-up could be explained hypothetically by ~~a significant increase in its liquid water content (LWC) caused by~~the evaporation of this light precipitation (Zouzoua *et al*., 2021). Nevertheless, our focus of this study is on the diurnal cycle of LLSC as influenced by aerosols alongside planetary boundary layer dynamics rather than examining the above hypothesis, which appeared to be related to a process beyond the local scale. Therefore, our model setting is made to specifically eliminate the influence of mid-cloud layer for the purpose as described later.

On 3 July 2016, the ATR-42 flew around Savè supersite and probed the boundary layer around 10:00 UTC. The ~~measurements confirmed~~airborne instruments detected ~~an important~~ aerosol size distributions with ~~number concentration with~~ a maximum ~~of~~ number concentration around 3500 cm^{-3} mainly ~~located~~ in the Aikten mode. The ATR-42 also detected an export of polluted airmass ~~ion~~ from Lomé (a coast city), which could explain the measured high~~er~~ ~~loading of~~ aerosol concentration in the Aikten mode (Denjean *et al*., 2020a). The measured aerosol chemical composition was mainly dominated by organics (55.3%), followed by sulfates (24.5%), ammoniac (11.2%), and nitrates (6.2%), while ~~little~~ only a small amount of BC mass was detected around Savè (2.8%). However, ~~these data are directly extracted from DACCIWA database, and~~ the measured aerosol size distributions ~~has to be~~were found to need a correction~~ed~~ ~~from~~ based on ~~the~~ aerosol refractive index to avoid bias. For this purpose, Denjean *et al*. (2020a) provided corrected profiles for ~~different typical~~various types of aerosol populations ~~encountered~~ measured during the DACCIWA campaign.

2.3 Meso-NH Model

In this study, we have simulated the observed case using the ~~French model~~ Meso-NH model (Lac *et al*., 2018). Meso-NH is a non-hydrostatic atmospheric research model that has been applied to studies in different scales ranging from synoptic to turbulent. Deployed in a limited area, the model uses advanced numerical techniques like monotonic advection schemes for scalar transport, and fourth order ~~WENO~~ advection scheme for momentum (Jiang and Shu, 1996). Sub-grid turbulence is parametrized using turbulence kinetic energy (TKE) based on Deardorff turbulent mixing length. In this study, ~~A~~ a fourth order advection scheme CEN4TH, centered on space and time, is applied with a Runge-Kutta centered 4th order temporal scheme for momentum advection (Lunet yet al., 2017). Aerosol and chemistry are also well represented. Here, Meso-NH version 5.4.2 is used and the relevant component modules and parametrizations for this study are described as follows.~~:~~

The aerosol-cloud framework of Meso-NH version used in this study is LIMA (Liquid Ice Multiple Aerosol)~~-~~. LIMA includes~~is~~ a complete two-moment scheme ~~(Vié *et al*., 2016)~~ predicting both the mass mixing ratio and the number concentration of aerosol species (Vié *et al*., 2016),~~-~~ using a superimposition of several aerosol modes, with each mode defined by its chemical composition and size distribution. Aerosols can act as either Cloud Condensation Nuclei (CCN) or Ice Forming Nuclei (IFN). Based on the ICE3-ICE4 ice microphysics schemes (Caniaux *et al*., 1994; Pinty and Jabouille, 1998; Lascaux *et al*., 2006) and the two-moment warm microphysical scheme C2R2 ~~from~~ (Cohard and Pinty, 2000), LIMA also predicts the number concentration of cloud droplets, raindrops, and pristine ice crystals. ~~It includes a prognostic representation of aerosol population using a superimposition of several aerosol modes with each mode defined by its chemical composition, size distribution and aerosols can act as a Cloud Condensation Nuclei (CCN) or an Ice Freezing Nuclei (IFN).~~ For modeling boundary layer cloud in ~~LESs~~LES mode, a pseudo-prognostic approach for supersaturation was developed (Thouron *et al*., 2012) to limit the droplet concentration production and to ~~so it would~~ represent cloud-top supersaturation better. A variant to C2R2, called KHKO, was developed by Geoffroy *et al*. (2008) for clouds producing drizzle following Khairoutdinov and Kogan (2000) parametrization. The~~se~~ clouds suitable for KHKO are thin and thus low precipitating warm clouds~~, and not sufficiently thick to produce heavy rain~~. The precipitating hydrometeors are drizzle only and their diameter are of the order of several dozens of micrometers. These modifications for KHKO were brought inside LIMA warm phase in order to better represent drizzle.

~~ECMWF radiation module, originated from ECMWF and based on two-stream methods, calculates the atmospheric heating rate and the net surface radiative forcing. Longwave radiation scheme used is Rapid Radiation Transfer Model (RRTM; Mlawer *et al*., 1997), based on the correlated k-distribution method. It integrates 16 bands and 140 g points (Morcrette, 2002). The shortwave scheme uses the photon path distribution method (Fouquart and Bonnel, 1980) in six spectral bands. Fluxes are calculated independently in clear and cloudy portion before being aggregated. The liquid cloud effective radius is computed from the liquid water content with the Martin *et al*. (1994) parametrization.~~

To better represent aerosols, we have used the aerosol module ORILAM (Organic Inorganic Lognormal Aerosols Model) in this study and ~~is an aerosol module~~ coupled it with~~to~~ Meso-NH ~~and~~ to interconnect the cloud microphysics module with ~~connected to~~ LIMA (Tulet *et al*., 2005). ~~It~~ ORILAM describes the size distribution and the chemical composition of aerosols using two lognormal functions respectively for the Aitken and accumulations mode~~s~~. These modes are internally mixed. ~~and f~~For each of them, the model computes the evolution of the primary species (black carbon and primary organic carbon)~~-~~, three inorganic ions (NO_3^-, NH_4^+,SO_4^{2-}), and condensed water. ORILAM includes a Second Organic Aerosols (SOA) module (Tulet *et al*., 2006) that is, however, ~~but are~~ not ~~taken into account~~included in this study. Three moments (the zeroth, third, and sixth) are considered for each mode to compute the evolution of total number, median diameter, and geometric standard deviation. Note that the choice of the 6th moment is numerical since it allows one to calculate the coagulation coefficients explicitly and to facilitate the integration of the aerosol solver. The size distribution can evolve through a particle coagulation process with both ~~intramodal~~ intra- and intermodal calculations. It can also evolve through condensation and merging between modes. ORILAM includes the CCN activation scheme of Abdul-Razzak and Ghan (2004) in order to replace the one of LIMA to calculate the number of activated CCN. ~~The others LIMA parametrizations in warm phase like the calculation of drizzle remain active.~~ The use of ORILAM needs to activate the gas phase chemistry scheme of Meso-NH (Tulet *et al*., 2003; Mari *et al*., 2004) using the EXQSSA solver. ORILAM has a nodule for gas-particle thermodynamic equilibrium (EQSAM for inorganics and MPMPO for organics) that allows the model to calculate the contents of inorganic and organic compositions including water within the aerosol (*e.g*., Metzger *et al*., 2002; Griffin *et al*., 2003). The solver will combine moment 0 (integrated number) and 3 (integrated new volume which integrates the hygroscopic growth) to calculate the new dimensional distribution (Tulet et al., 2005, 2006). ~~Inorganic chemistry system (EQSAM, Metzger et al. (2002)) solves the chemical composition of sulfate-nitrate-water-ammonium aerosols based on thermodynamics equilibrium.~~ ~~For secondary organic aerosols, the thermodynamic equilibrium uses the MPMPO scheme from Griffin *et al*. (2003).~~ ORILAM directly computes the evolution of aerosol extinction, SSA, and asymmetry factors that are coupled online with the radiation scheme of Meso-NH for the 6 short wavelengths from the aerosol chemical composition and size parameters (Aouizerats *et al*., 2010).

ECMWF radiation module is adopted in this study. Based on the two-stream method, this module calculates the atmospheric heating rate and then net surface radiative forcing. Longwave radiation scheme used is the Rapid Radiation Transfer Model (RRTM; Mlawer *et al*., 1997), based on the correlated k-distribution method. It integrates 16 bands and 140 g points (Morcrette, 2002). The shortwave scheme uses the photon path distribution method (Fouquart and Bonnel, 1980) in six spectral bands. Fluxes are calculated independently in clear and cloudy portions before being aggregated. The liquid cloud effective radius is computed from the liquid water content with the Martin *et al*. (1994) parametrization.

The surface model used in our modeling is the SURFEX, which is a standardized surface module containing surface schemes externalized of Meso-NH (Masson *et al*., 2013). ~~Each~~ With SURFEX, each grid point can be split into four tiles: land, town, sea, and inland water (lake, rivers). In case of a shrubs ~~typical~~ surface, the interactions between soil, biological processes, and atmosphere are calculated by ISBA parametrization (Noilhan and Planton, 1989). ~~It represents the effect of vegetation and bare soil.~~ Several ~~evapotransipration~~evapotranspiration formulations are available for simulating plants and ~~for simulating the~~ CO_2 fluxes. Soil is represented as a bucket of two or three layers. The land tile can be separated into as many as ~~up to~~ 19 subtiles following the type of vegetation.

2.4 Model settings

Based on the observations and the capability of the model, a reference case (REF) was first designed to simulate ~~through~~ in LES. The reference case serves as a base to reproduce the major features of the observed LLSCs ~~diurnal~~ life cycle particularly ~~under~~ using an observed aerosol profile. It also serves as a reference for further sensitivity simulations with different aerosol configurations to study the impacts of aerosol composition alongside abundance on LLSCs.

The domain is a 3D box of 9.6 km x 9.6 km x 2 km in size, with a horizontal resolution of 40 m x 40 m. Note that the radiation module still proceeds calculations above 2 km using prescribed profiles. The vertical resolution is 10 m between 0 m and 1200 m then 40 m above until 2 km of altitude~~. Such high resolution is able~~ to resolve explicitly the ~~biggest~~ important turbulent eddies. A periodic boundary condition on the horizontal directions is applied and an absorbing layer is set ~~at~~ between 1.8 and 2 km height. A thermodynamic perturbation is deployed to activate turbulence at the beginning of the simulation at 23:00 UTC of 2 July and the spin-up is 1h (though observed clouds formed around 02:00

UTC). A subsidence profile is applied following Bellon and Stevens (2013) scheme $w_{subs}(z) = -w_0[1 - \exp(-z/z_w)]$, with $w_0 = 15\ mm\ s^{-1}$ and $z_w = 250\ m$. This subsidence profile is applied during the entire simulation to keep a nearly constant cloud top height during the stratus phase and to better control the convective phase. The surface energy and water fluxes are simulated by SURFEX ISBA scheme, parametrized ~~by~~ using data from Savè supersite, ~~measurements~~ with the typical vegetation ~~around of Savè which~~ consisting~~s~~ of shrubs, crops, or taller trees, assuming a flat surface ~~corresponding to~~in the area around Savè. A time-step of 2s is used, which appears to be adequate based on testing runs to study ~~accurately~~ the LLSCs nocturnal-diurnal variations particularly involving aerosol and cloud microphysics. ~~Note that t~~The radiation scheme is called every 10 minutes. Note that previous studies regarding nocturnal stratus-stratocumulus suggested that a vertical resolution as fine as 5 meters near the cloud top would be necessary for reproducing the cloud top entrainment and thus cloud macrophysical structures (Stevens *et al.*, 2005). ~~Since~~ However, the nocturnal-diurnal life cycle in our case involves a dynamically evolving cloud top ~~(~~from 400 to 1200 m, particularly in the daytime~~)~~, ~~it makes~~making it a difficult task to prescribe a highlighted zone for finer resolution. Our fast-testing results, on the other hand, did not suggest an alarming difference between the run with 10 m and 5 m vertical resolution (not shown). Therefore, the current vertical resolution and the time step are selected to well cover all possible cloud tops during the simulation ~~time~~ and to provide ~~the~~ a best economic computational performance for modeling aerosol-cloud interaction with a fully coupled chemistry model.

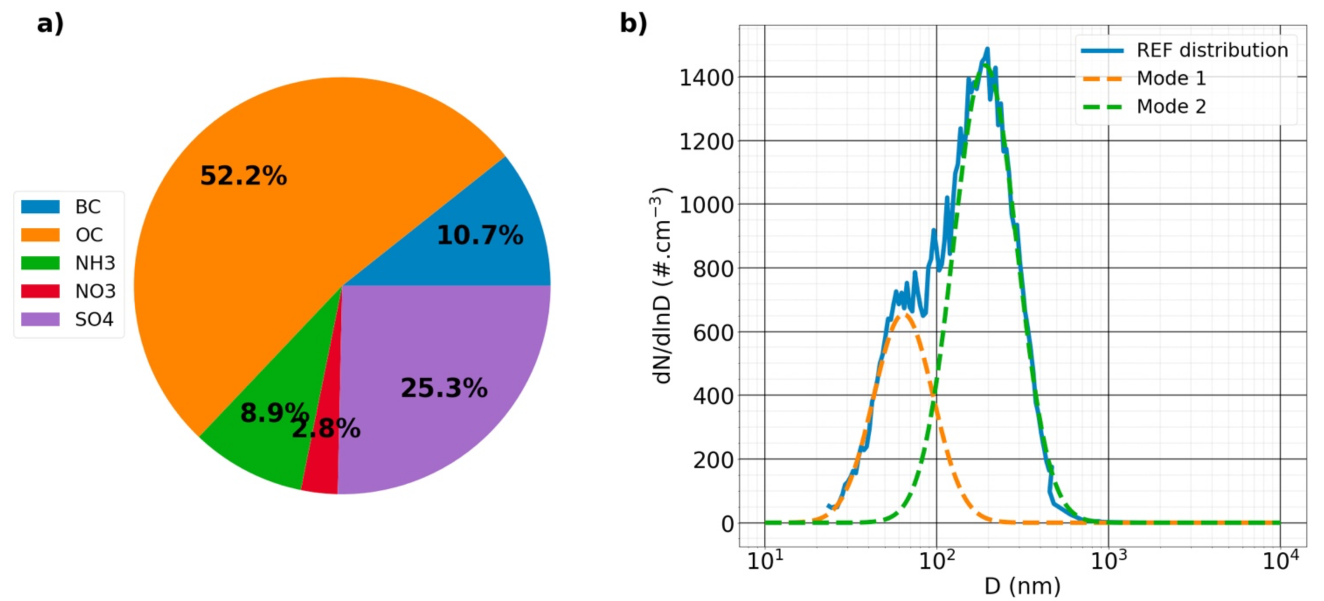

Figure 3. Aerosol chemical mass compositions (a) and size distribution fitted into 2 modes described in Table 1 (b) used in REF.

	$N_a\,(cm^{-3})$	σ	D (nm)
Mode 1	654	1.49	63.98
Mode 2	1530	1.53	190.97

Table 1. REF aerosol size distribution described by two modes configured by three parameters (number concentration N_a, standard deviation σ and diameter D).

REF case is configured using the radiosondes of 2 July at 23:00 UTC for temperature, humidity, and horizontal wind components (U, V). The simulation is then controlled by tendency profiles of temperature, humidity, and horizontal wind applied homogeneously on the domain each hour. These tendency profiles are based on the hourly radiosondes launched on 3 July between 00:00 and 11:00 UTC. After 11:00 UTC, the next tendency profiles were designed based on the measurements of the microwave radiometer, the analysis of surface incoming solar radiative flux, and the cloud thickness and cover. Note that, despite these best possible efforts in configuring a set of observation-constrained tendency profiles to reproduce observed cloud field, it is difficult to eliminate the possibility that such profiles could reflect certain local thermodynamic effects however small they are. In practice, our ~~principal~~ main goal is to make the profiles to be able to force the modeled clouds reproduce observed quantities of major features such as cloud top, base, liquid water path (LWP), surface incoming solar radiation, among others, in the REF case. This would serve the best purpose for us to address the major issue of this study, *i.e.*, the role of different aerosol profiles in the ~~diurnal~~ life cycle of modeled LLSCs.

We ~~decided to~~ use a "background" distribution as the aerosol profile for REF simulation. This profile, as described in Denjean *et al*. (2020a), ~~actually reflects~~reflects the influence of aged BBA on clouds with minor influence of local anthropogenic sources. The aerosol number size distribution is dominated by a particle accumulation mode centered at 190 nm and a smaller Aiken mode centered at 64 nm ~~as seen in~~(~~-~~Figure 3b). This profile exhibits a high loading of aerosols with a maximum of 1400 cm^{-3} detected in the accumulation mode. The aerosol chemical composition ~~was~~ is dominated by organics (52.2%), followed by sulfates (25.3%), ammonium (8.9%), BC (10.7%), and nitrates (2.8%). The configuration of ORILAM has been initialized using the REF aerosol chemical composition and ~~number~~ size distribution given in Table 1 and Figure 3b by fitting the SMPS profiles into two lognormal modes using the "py-smps" package (Hagan *et al*., 2022), with each mode having the same chemical composition.

3. Analysis of REF Results

3.1 Simulated LLSCs evolution

The simulation of the REF scenario reproduces the formation of the observed LLSCs deck on 3 July 2016 as shown in Figure 4. The formation of clouds leads, as described in section 2.2, to the end of the jet phase. The domain mean CBH, estimated from the modeled mixing ratio of cloud droplets follows the ceilometer's measurements during the stratus phase between 02:00 and 10:00 UTC, varies~~ying~~ between 100 and 200 m of altitude. The simulated mean Cloud Top Height (CTH) evolves from 400 to 550 m of altitude, well within the range ~~of the values~~ from 500 to 580 m detected by the radar~~. D~~, though during the convective phase, the model result~~s~~ differs slightly from the observations. ~~Note that t o analyze the~~

~~cloud cover profile over the domain, the Cloud Presence Probability (CPP) at each model layer, differing from cloud fraction that is often defined as a column metrics, is calculated as a percentage of all cloud pixels with a total condensed water mixing ratio exceeding 0.05 g kg^{-1} at the given model layer (Fig. 4). Nevertheless, the~~The modeled mean simulated CBH and CTH are overestimated compared to ceilometer and radar values ~~in~~ during some periods ~~particularly~~ in late morning and afternoon. The difference between simulated and ceilometer detected CBH can ~~differ from ceilometer one by~~be as large as 150 m of altitude at 11:00 UTC. ~~The~~ While CTH is often overestimated by 100 m. Between 15:00 and 16:00 UTC, the simulated mean CBH approaches again the ceilometer readings (600 to 950 m) (no radar values are available to validate the simulated CTH). As mentioned in section 2.1, the ceilometer is a lidar while the ~~radar~~ values are derived from reflectivity vertical profiles ~~which have~~with a 30 m of resolution. The differences between the model and the observation between 13:00 and 16:00 UTC ~~are likely~~could come from~~due to~~ the different representation of simulated result (a domain average) versus that of ceilometer detection (limited to only one vertical direction)~~ing of the simulated values~~, ~~the tendency profiles established from corrected radiosonde values, the ceilometer values limited to only one vertical direction,~~ the vertical resolution of ~~radar~~ observed profiles, ~~or~~ the limitation of radar in detecting hydrometeors, and in the end, certain model weaknesses likely associated with a lack of hourly radiosondes during the afternoon period to provide sufficient observational constrain.

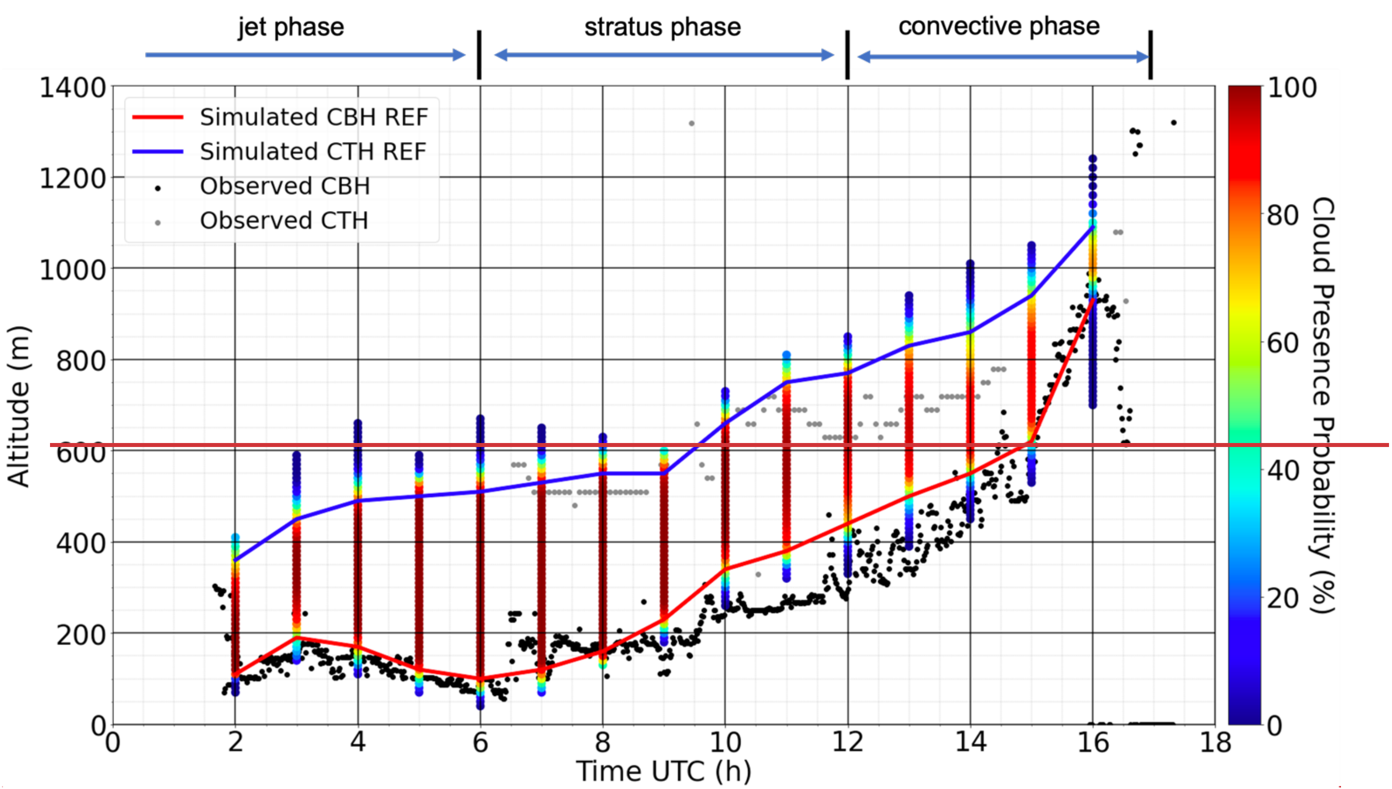

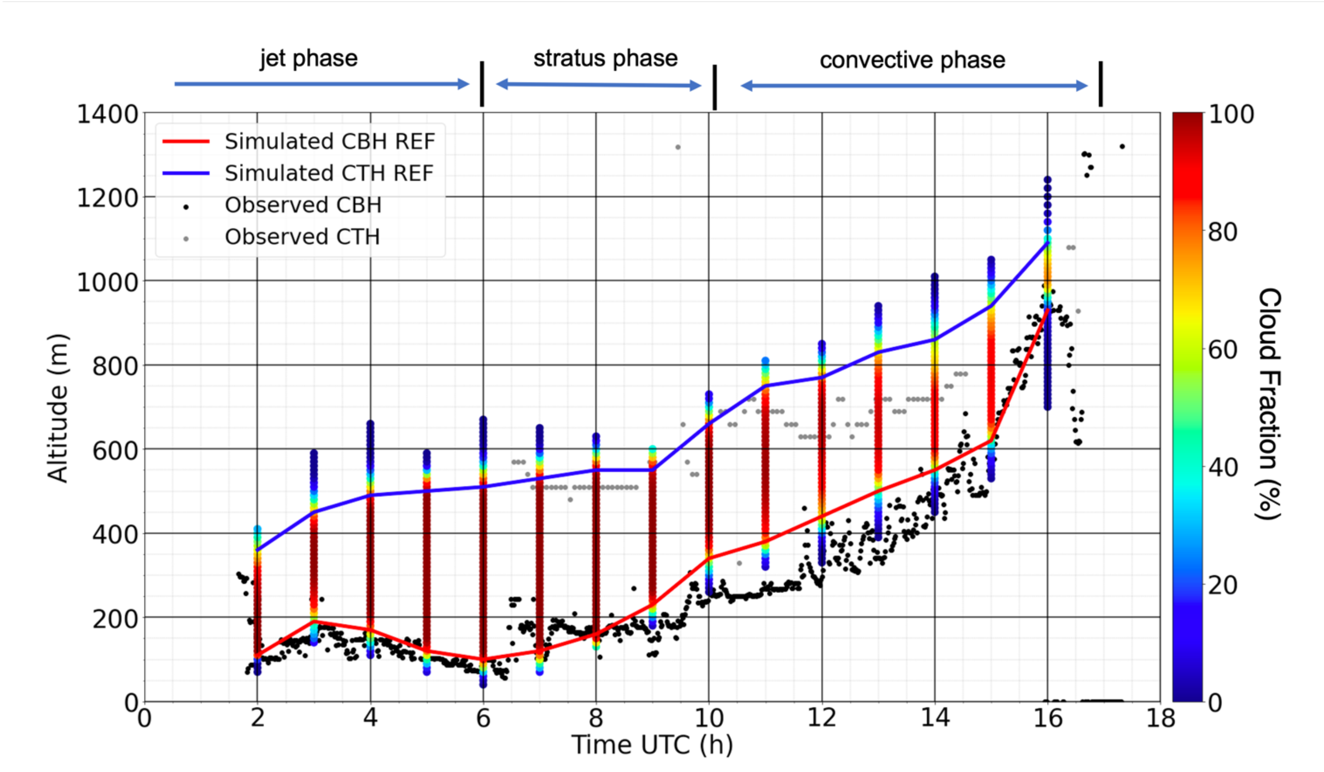

Figure 4. Simulated LLSCs deck evolution compared to Savè ceilometer and radar measurements, vertical color bars attribute cloud fraction in percentage at each altitude level~~ a modeled cloud presence probability~~. Here ~~mean ~~simulated CBH and CTH represent domain-averaged cloud base and cloud top height, respectively. Different phases might have overlaps; therefore, their marks only serve a reference purpose here.

To analyze the cloud cover profile over the domain, the cloud fraction (CF) at each model layer is calculated as the percentage of all cloud pixels with a total condensed water mixing ratio exceeding 0.05 g kg^{-1} at each given model layer (Fig. 4). Note that this cloud fraction differs from the cloud fraction defined as a column metric. In addition, Liquid W~~w~~ater P~~p~~ath (LWP) at each column (Fig. 5), calculated based on cloud pixels, brings a view on the horizontal organization and homogeneity of the cloud deck. During the stratus phase, the ~~CPP ~~CF is nearly equal to 100% between CBH and CTH, suggesting~~giving~~ a homogeneous cloud deck~~. The top~~ consistent with ~~panel of Figure 5 gives a comparison of the cloud organization in the model and from ~~cloud observations with sky camera (visible range) (Fig. 5, the top panels). Notably, peak LWP values between 06:00 and 12:00 UTC are quite close while domain-means differ (Fig. 5). In comparison, both peak and domain mean LWP are sharply lower at 16:00 UTC.

~~At 06:00 UTC, cloud deck covers the entire domain as seen in both modeled result and in observations (note the distinct cloud rolls in model results).~~ Between 10:00 and 13:00 UTC, ~~the ~~CF of the ~~CPP in ~~layers between domain mean CBH and CTH starts to decrease~~s~~ from near 100% to 90%, while CF at CBH and CTH~~. Near the two averaged values, CPP~~ decreases more substantially to reach near 60% and 80%~~ at CBH and CTH~~, respectively. This leads to a less ~~in~~homogeneous cloud deck confirmed by the LWP map and the observation of the sky camera at 12:00 UTC shown in the middle row of Figure 5. Indeed, more cloud-free pixels begin to appear between clouds, hence ~~and~~ sunlight is seen through the cloud deck by the cloud camera. Finally, ~~the CPP~~CF continues to decrease until the end of the convection phase with a maximum barely reaching 80%, and ~~a~~ values around ~~mean~~domain mean CBH and CTH level as low as 20% and 40%, respectively. This demonstrates the break-up of the cloud deck during convection and the cloud thinning. The bottom panels of Figure 5 show clearly the dissipation of a large number of clouds alongside substantially thinning of the others at 16:00 UTC~~ PM~~. ~~The LWP map (Fig. 5b) shows numerous thin clouds corresponding to those seen by the camera of Savè.~~

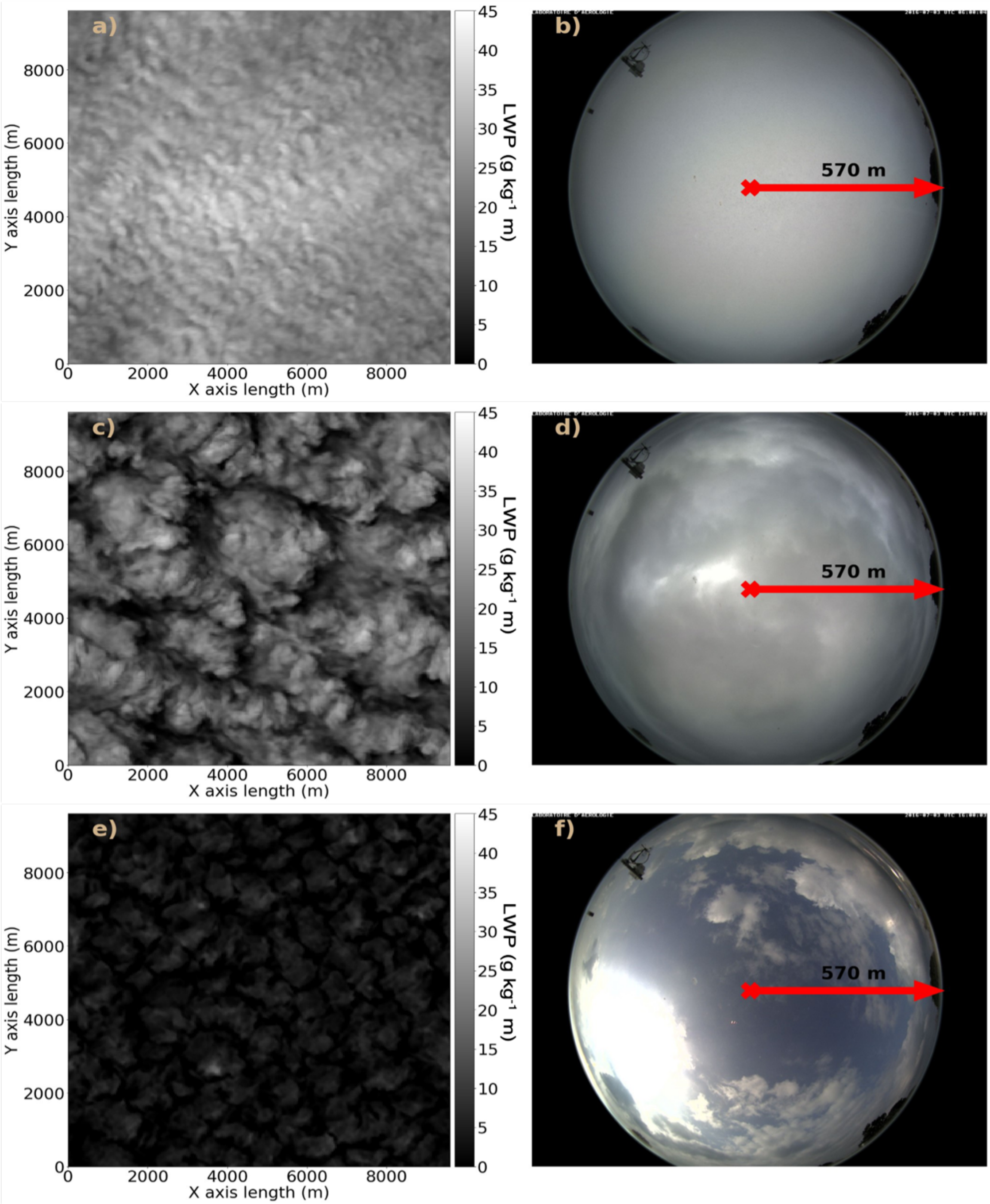
a)
b)
c)
d)
e)
f)
Y axis length (m)
X axis length (m)
LWP (g kg-1 m)
570 m
0
2000
4000
6000
8000
5
10
15
20
25
30
35
40
45

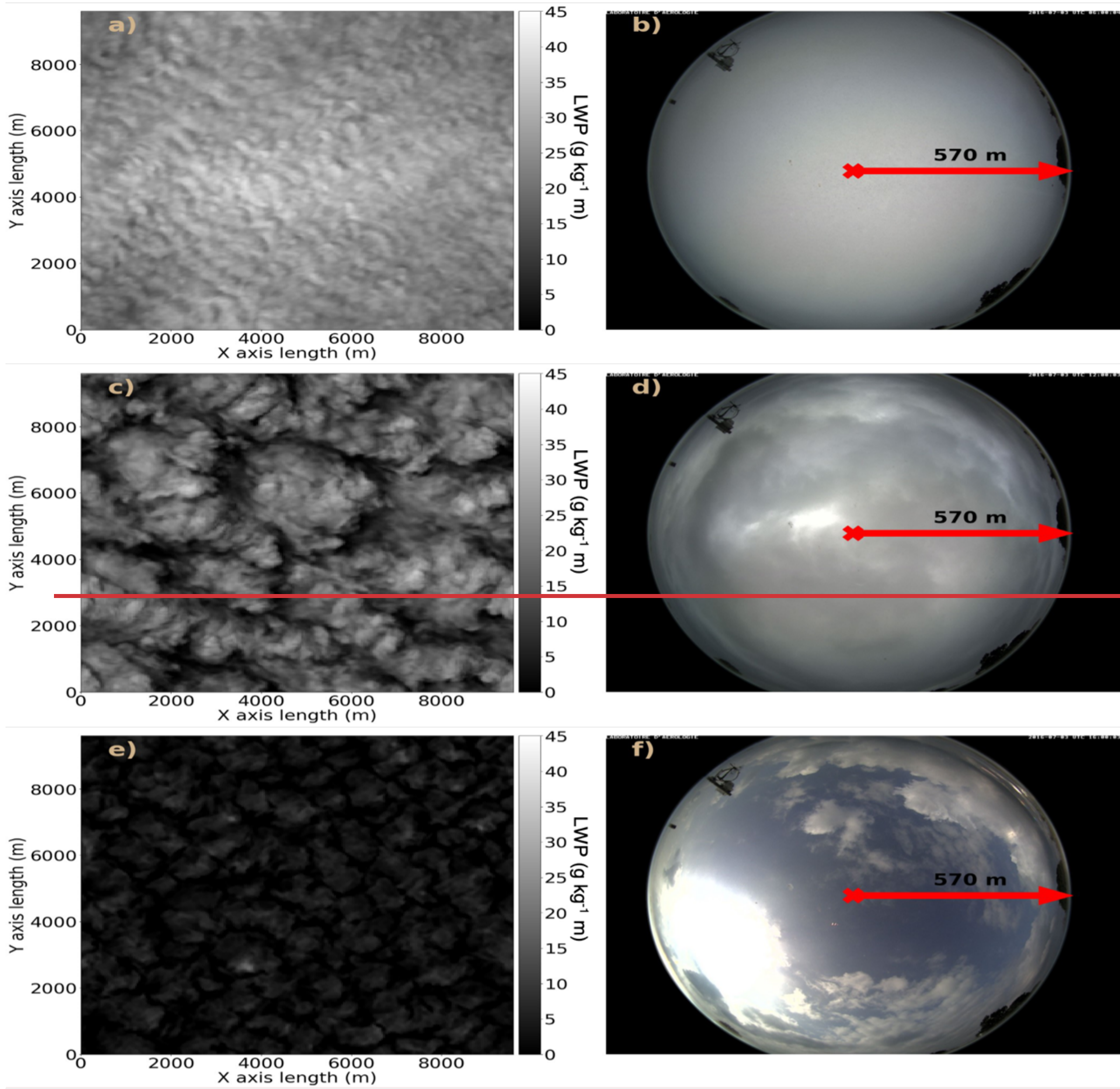

Figure 5. Comparison between modeled liquid water path (LWP, *g kg*$^{-1}$ *m*) and the images from Savè cloud camera at 06:00 (top), 12:00 (middle) and 16:00 UTC (bottom).

Figure 6a shows the comparison between the modeled domain-average shortwave (SW) radiation flux at the surface (SWRADSURF)~~, averaged over the modeled domain~~ and the corresponding measurements performed by the energy balance station. Observed values are fitted following the ~~locally~~ LOcally Weighted Scatterplot Smoothing (LOWESS) method (Cleveland, 1979)~~, which is a non-parametric regression method performing weighted local linear fits~~. The temporal evolution of the modeled SWRADSURF follows the observations rather well ~~although~~ despite some biases~~ can be observed~~. After 06:00 UTC the solar radiation reaches the ground ~~and~~ as the cloud deck thickness and covering show little variations.~~,~~ ~~the~~ Thereafter, the radiative flux increases gradually by reaching near

200 $W\,m^{-2}$ at the end of the stratus phase (10:00 UTC). As clouds deck becomes inhomogeneous during the convective phase (10:00 to 16:00 UTC), the modeled surface solar flux reaches a maximum of 300 $W\,m^{-2}$, which is a bit ~~less~~ lower than the fitted 350 $W\,m^{-2}$ value from measurements. ~~Finally, w~~When the clouds break up further, more solar radiation can reach the surface~~,. After this period during~~ ~~which~~ and model and observation~~s~~ agree well thereafter with an exception at~~,~~ ~~from~~ 15:00 UTC, where the mean modeled curve decreases to 200 $W\,m^{-2}$ while the fit observed curve is near 320 $W\,m^{-2}$ due to an overestimation of the cloud thickness by the model. At 16:00 UTC, both modeled and measurement values are very close ~~at~~ around 280 $W\,m^{-2}$. Generally, the modeled maximum values are higher than the ones detected by the Savè ground instrument. ~~For example, at 10:00 UTC, the balance detected a peak of 300 $W\,m^{-2}$ while the model value reached near 400 $W\,m^{-2}$.~~

Figure 6b and 6c show~~s~~ that the evolution~~s~~ of the modeled domain-mean latent and sensible heat flux~~es~~ reproduce~~d~~ those measured by the instrument rather well. During the night, the sensible heat flux ~~was~~ is negative then increases~~d~~ to 0 $W\,m^{-2}$ close to the sunrise time (06:00 UTC), indicating a reduction of the cooling close to the ground (Dione *et al*., 2019). Between 09:00 and 14:00 UTC, the modeled ~~two~~ sensible and latent heat flux~~es~~ follow~~ed~~ the measured trends though with an overestimate~~d~~ ~~by~~ of almost 70 and 18 $W\,m^{-2}$, respectively.~~.~~ Then the ~~mean~~ modeled curves go below the fitted observed curves at 15:00 UTC and finally both merge ~~decrease~~ to almost 0 $W\,m^{-2}$ after 18:00 UTC. The difference between modeled and observed ~~latent and sensible~~ heat fluxes may be again due to the different representations of area, as modeled quantities are domain-mean values while measurements are at a single point. ~~covered by the measurements and the model and the prescribed subgrid-scale distributions of cloud droplets.~~

In Summary, the REF simulation has successfully reproduced the major observations obtained by the instruments at Savè on 3 July 2016. ~~The~~ For example, the modeled cloud thickness and coverage ~~represent~~ reflect ~~well~~ the measured cloud ~~situation~~ macrophysical status ~~with~~ despite some ~~inaccuracies~~ discrepancy, likely due to ~~the~~ a lack of hourly radiosonde data ~~and~~ to ~~in~~sufficiently ~~correction of~~correct the tendency profiles ~~applied all along the~~to cover the entire simulation period particularly in afternoon hours~~to control temperature and humidity every hour~~. The modeled ~~heating of the ground by~~ solar radiation at ground also follows the measurements ~~of the energy balance of Savè~~very well except for ~~and maximum variation on the domain are a bit~~ certain overestimates~~overestimated~~. ~~The~~ In addition, the sensible and latent heat fluxes ~~detected~~ measured at Savè have also been well captured by the model.

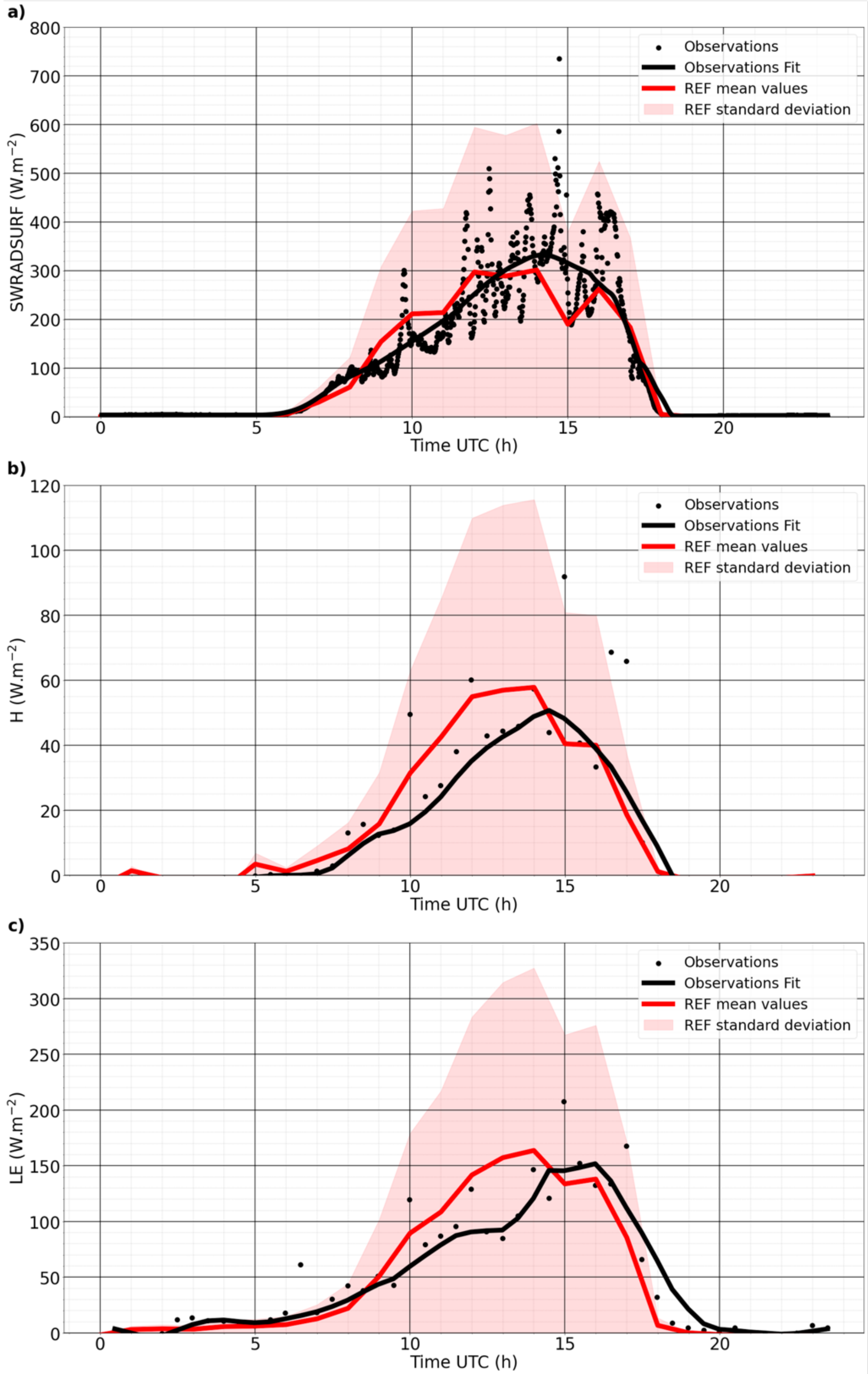

Figure 6. Comparison between Savè surface observation and REF simulation for SW radiation flux at surface (SWRADSURF,a), sensible heat flux (H, b) and latent heat flux (LE, c) all expressed in $W\,m^{-2}$ at the surface. The variation of REF for each parameter indicates the range of possible values these parameters can take.

3.2 Thermodynamic, dynamical, cloud microphysical, and radiative analyses

Thermodynamic, dynamical, and radiative processes and their interaction with cloud microphysics are among the key factors in determining the life cycle of LLSCs. Here we discuss the evolutions of these processes simulated by the model in the REF case ~~in order to~~to better understand the reasons behind model-observation consistency or discrepancy. The discussion will be emphasized ~~in~~ on three periods. The first period is the transition between jet and stratus phase (between 00:00 and 04:00 UTC) to observe ~~how clouds are formed~~the formation of the clouds. The second period is the stratus phase between 06:00 and 10:00 UTC, ~~because of the stability of the~~ when the stable cloud layer was observed by instruments ~~of~~ at Savè. The third period is the convective phase between 12:00 and 17:00 UTC to study how the properties of LLSCs evolve during the break-up stage.

3.2.1 Transition jet-status phase

~~The formation of clouds is controlled by the temperature and humidity tendency profiles established from the radiosonde measurements made on the 3rd of July 2016.~~ Figure 7 gives modeled domain-averaged profiles of selected macro- and microphysical features~~the simulated temperature (T) and relative humidity~~ for the transition of jet to status phase~~. As explained in section 2.2,~~, when maritime inflow already reached the site~~, increasing humidity and creating NLLJ~~. ~~Temperature decreased from 24°C to 23°C at ground from 00:00 to 04:00 UTC and from 24°C to 21°C near 400 m of altitude. The~~ As expected, the advection of cold and slightly humid air leads to ~~the~~ an increase of relative humidity (RH) ~~as expected~~to reach~~ing~~ 100% at 02:00 UTC at 100 m above ground. After this time, RH exceeds saturation between 100 and 500 m of altitude. The inversion occurs around 325 m and 500 m respectively at 02:00 UTC and at 04:00 UTC. The NLLJ is well represented in modeled results as the mean wind speed (w_s) before cloud formation is greater than 7 $m\ s^{-1}$. After cloud formation, the NLLJ core nearly corresponds ~~near~~ to the mean cloud base height (Adler *et al.*, 2019; Babic *et al.*, 2019; Lohou *et al.*, 2020). The turbulence during this period is shear-driven due to this NLLJ,′ ~~which~~ yielding~~s~~ a well-mixed sub-cloud layer. The turbulent kinetic energy (TKE) is high above ground (0.5 to 0.2 $m^2\ s^{-2}$), then decreases to near zero above rough 200 meters at 00:00 UTC. After 02:00 UTC, TKE increases at the level of ~~the~~ CTH (350 and 500 m) and decreases at the center of clouds (0.04 $m^2\ s^{-2}$), indicating this area is less turbulent than the extremities of the cloud layer.

Cloud droplet number concentration or CDNC (N_c) is determined by the supersaturation in an updraft at cloud base and the concentration of aerosols that activate at this~~eir~~ supersaturation. In Figure 7e, simulated aerosol concentration~~s~~ ~~were~~ is the highest close to the ground ~~and~~ then ~~decreased~~ decreases with altitude up to around 2 km. This simulated aerosol profile is similar to ~~those~~ the ~~observed by~~ airborne measurements during DACCIWA (Taylor *et al.*, 2019; Denjean *et al.*, 2020a~~) with locally emitted aerosols transported above the boundary layer due to a combination of land-sea surface temperature gradients, orography-forces circulation and the diurnal cycle of the wind along the coastline (~~; Deroubaix *et al.*, 2019; Flamant *et al.*, 2018). The simulated cloud microphysical features~~s~~ reflect~~s~~ a polluted condition~~s~~ ~~with~~ as N_c reaches~~ing~~ 1750 *droplet* cm^{-3} and mean cloud droplet radius r_c around 5 μm ~~which~~ that is not enough to form ~~even~~ drizzle (size between 0.2 mm and 0.5 mm;~~,~~ ~~(~~Pruppacher *et al.*, 1998; Sandu *et al.*, 2008~~)~~). These values are in the range of ~~those~~ corresponding measurements~~d~~ ~~inland~~ at the same altitude by Taylor *et al*. (2019)~~ during DACCIWA~~. ~~Median~~ The median of simulated CDNC ~~was~~ is 500 *droplets* cm^{-3} at the beginning of cloud formation ~~and~~ then ~~reached~~ reaches 1750 *droplets* cm^{-3} ~~latter~~later, most likely due to the continuous activation of aerosol into cloud droplets.

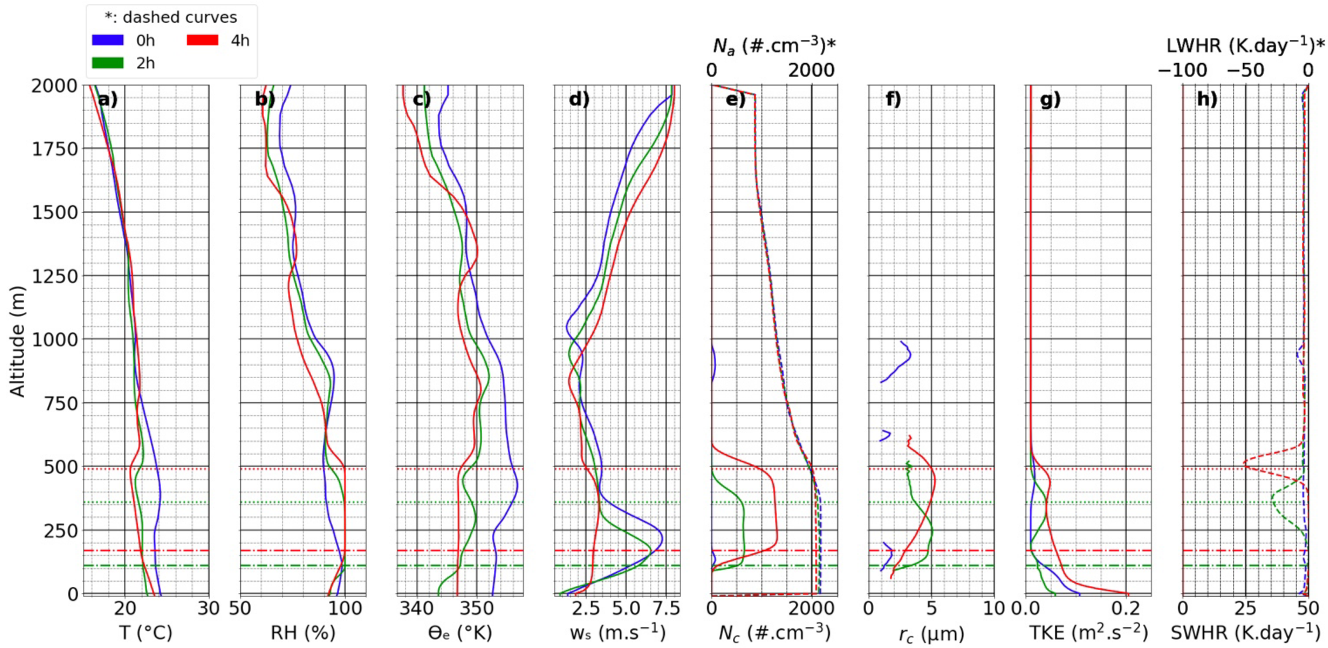

Figure 7. Profiles from left to right of temperature (T, a), relative ~~humidty~~humidity (RH, b), equivalent potential temperature (θ_e, c), horizontal wind speed (w_s, d), aerosol number concentration (N_a, dashed curve, e), cloud droplets number concentration (N_c, plain curve, e), mean cloud droplet radius (r_c, f), turbulent kinetic energy (TKE, g), longwave heating rate (LWHR, dashed curve, h) and shortwave heating rate (SWHR, plain curve, h) at 00:00, 02:00 and 04:00 UTC. ~~Dashdot~~The horizontal dashed dot ~~horizontal~~ lines represent mean cloud base height (CBH) and dotted horizontal lines the mean cloud top height (CTH).

The emission of thermal radiation by the clouds during the stratus phase creates a cooling at the cloud top as demonstrated by the ~~profiles~~ evolution of modeled ~~the~~ Long-Wave Heating Rate (LWHR) profiles at Figure 7h. The more numerous the cloud droplets are the stronger the cooling is, as shown in Fig. 7h that ~~Short-Wave Heating Rate (SWHR)~~LWHR can reach −50 *K* day^{-1}. This strong longwave emission ~~is able to~~can reduce the thermal production of turbulence above the cloud top, deepening the temperature inversion. A stabilized cloud top layer by radiative cooling and a NLLJ core contributing to the shear-driven turbulence below the cloud base ~~allows the~~leads to a ~~well-mix~~well-mixed~~ing of the~~ cloud layer, making the LCL to correspond to the LLCSs base as seen in~~at~~ Figure 2 (Adler *et al*., 2019; Lohou *et al*., 2020).

3.2.2 Stratus phase

The stratus phase starts just after the sunrise. ~~To m~~Maintaining stratus in almost the same state ~~as in the previous period~~throughout this phase needs certain proper temperature and humidity conditions. A~~a~~s shows in (Figure 8),~~.~~ between 06:00 and 08:00 UTC ~~Indeed,~~ the ground temperature ~~is stil~~varies little~~l~~ ~~at~~ around 23°C ~~at 06:00 and 08:00 UTC~~, ~~and 20°C at the mean CTH (500 and 550 m respectively). RH profiles indicate that~~ supersaturation still exists between ~~the range of~~ CBH and CTH~~, allowing droplets condensation to continue.~~ , and a~~A~~ir masses are quite well-mixed within ~~PBL during this time~~ as θ_e is near constantly ~~equal to~~at 347 K throughout the boundary layer and the inversion layer is settled where θ_e is reaching 350−351 K. The horizontal wind speed between the ground and the cloud base decreases, which indicates ~~the~~ a ~~reducing~~weakening ~~of the~~ NLLJ core (nearly 2 $m\ s^{-1}$), ~~and it~~then rises ~~in~~ with altitude due to the turbulent mixing induced by the LW cooling at the cloud top during the night. The turbulence between ground and cloud center decreases to 0.03 $m^2\ s^{-2}$ then finally increases slightly to 0.04 $m^2\ s^{-2}$ at the mean CTH. The TKE is a bit stronger at 08:00 UTC, reaching 0.05 $m^2\ s^{-2}$ in the cloud layer, ~~which is explained by~~implying an increase of ~~the vertical wind speed~~surface solar heating.

The aerosol concentration at 06:00 and 08:00 UTC is around 2000 cm^{-3} up to 500 m altitude, then ~~it~~ decreases along altitude. This concentration is ~~still~~ high enough to ~~allow the formation of~~sustain a CDNC of 1100−1200 $droplets\ cm^{-3}$ between CBH and CTH. The concentration of cloud droplets leads to a maximum layer-mean droplet radius of 6 μm, which is still not enough to form drizzle. The cloud layer has an albedo close to 1 due to the high ~~droplet concentration~~CDNC. The presence of light absorbing aerosol ~~causes the shortwave that causes~~amplifies the Short-Wave Heating Rate (SWHR) ~~amplified~~ at the cloud top by semi-direct effect. At 08:00 UTC, the SWHR and LWHR are equal to 27 $K\ day^{-1}$ and −70 $K\ day^{-1}$, respectively.

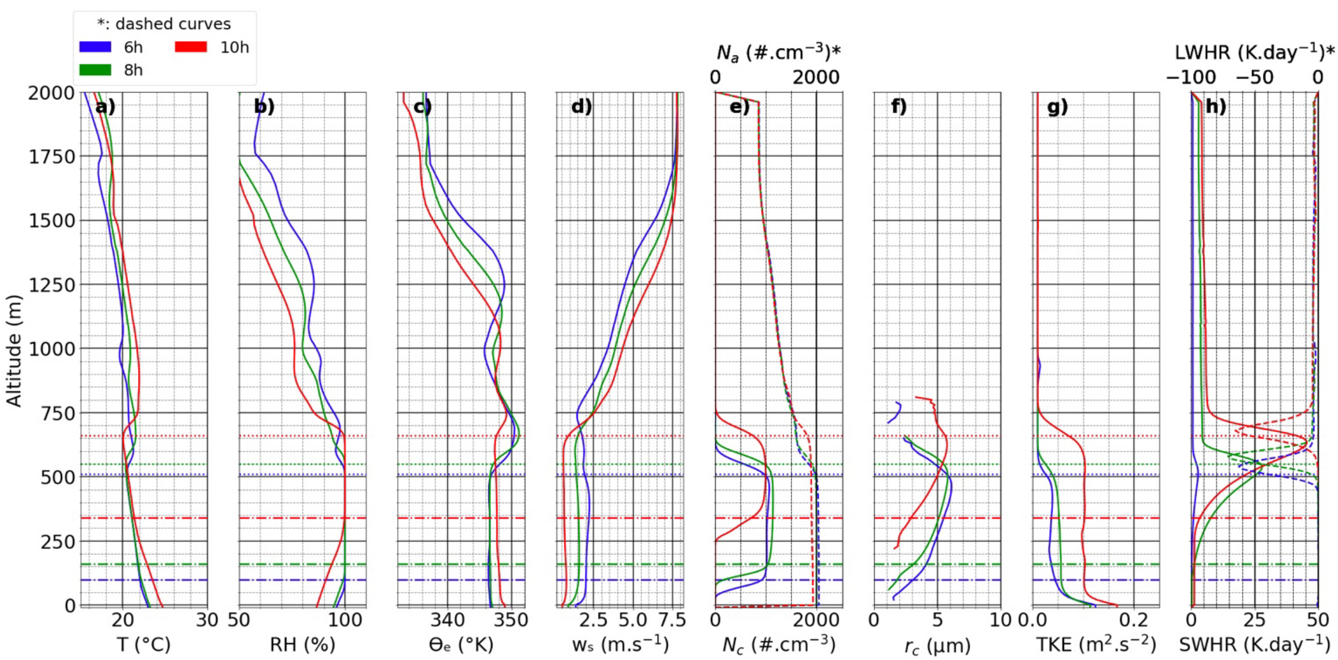

Figure 8. Profiles from left to right of temperature (T, a), relative humidity (RH, b), equivalent potential temperature (θ_e, c), horizontal wind speed (w_s, d), aerosol number concentration (N_a, dashed curve, e), cloud droplets number concentration (N_c, plain curve, e), cloud droplet radius (r_c, f), turbulent kinetic energy (TKE, g), longwave heating rate (LWHR, dashed curve,

h) and shortwave heating rate (SWHR,plain curve, h) at 06:00, 08:00 and 10:00 UTC. Dashdot horizontal lines represent mean cloud base height (CBH) and dotted horizontal lines the mean cloud top height (CTH).

At 10:00 UTC, the cloud layer starts to rise significantly, with CBH and CTH reaching 340 and 660 m, respectively. Moreover, stronger solar irradiance ~~can~~ reaches the ground (220 $W\ m^2$), leading to the heating of the surface and the increasing of the sensible and latent heat fluxes as seen in Figure 6. It also increases the temperature near ground to 24 $°C$ and at the cloud top ~~the temperature is~~to 20 $°C$. ~~Supersaturation occurs obviously between cloud base and cloud top and t~~The inversion layer is observed above the cloud top between 660 and 750 m. The NLLJ core is no longer present ~~as the horizontal wind speed decreased to 0.5–0.75 $m\ s^{-1}$~~. ~~However, the turbulent kinetic energy~~TKE increases to 0.1 $m^2\ s^{-2}$ throughout the vertical layer from 50 meter above the ground to a level just below the cloud top. This enhancement of turbulence is expected to increase entrainment entering the cloud from above as well. ~~Clouds are having a maximum of 1000 cm^{-3} and a maximum droplet radius reaching near 6 μm. Given these values, the cloud albedo is near equal to 1 and t~~The SWHR increases to 45 $K\ day^{-1}$, ~~. It~~ almost compensates the LWHR ~~value~~ cooling of 65 $K\ day^{-1}$. ~~During the 3rd of July, the radar detected light precipitation from higher clouds but this simulation doesn't model this type of clouds. So, the cloud deck stands longer due to the set-up of tendency profiles especially the one for humidity which keeps supersaturation at stratus layer until 10:00 UTC.~~

3.2.3 Convective phase

This phase ~~is extending~~extends from 12:00 to 17:00 UTC ~~in~~on 3 July 2016~~ case~~. During this period, ~~when the~~surface SW radiation flux ~~at surface~~ is maximized at 300 $W\ m^{-2}$ (Figure 6), leading to ~~a~~an ~~more~~ intense surface heating ~~from the surface~~. ~~During this period~~As a result, the ground temperature ~~at ground~~ evolves from 25 to 27 °C as seen at Figure 9~~. The temperature near the cloud top is 20°C at 12:00 and 14:00 UTC. At the break-up time (16:00 UTC), the temperature is lower than 18°C at the CTH. The formation of clouds is possible due to RH exceeding 100% in upper altitude, as the c~~Convection of humid air masses causes the CBH and CTH to rise from 450 to 925 m and from 760 to 1100 m, respectively. The formation of clouds is still possible due to RH exceeding 100% in upper altitude. Moreover, at ~~the break-up (~~16:00 UTC~~)~~, the equivalent potential temperature decreases above 450 m of altitude, indicating air masses become more unstable with altitude. The horizontal wind speed is weak at the beginning of the phase with 0.5 $m\ s^{-1}$ at ground level but increases along time to reach 1 $m\ s^{-1}$ at ground and 3 $m\ s^{-1}$ around 700m. This increase coincides the dissipation of the LLSCs and indicates the arrival of the marine inflow.

The turbulence profiles evolve along altitude during the convection phase, reaching 0.075 $m^2\ s^{-2}$ in center of clouds and almost zero near 850 m at 12:00 UTC. ~~This profile evolves at~~By 14:00 UTC, TKE ~~to~~ reaches 0.25 $m^2\ s^{-2}$ inside the cloud~~and zero at cloud center and 1000 m~~, indicating a reinforcement of turbulence ~~due to an elevation of dynamical production via the vertical wind speed increase~~. ~~Finally a~~At ~~break-up time~~16:00 UTC, ~~turbulence~~ TKE ~~near the ground~~ decreases near the ground but increases at cloud level ~~the TKE has~~to a value of 1.5 $m^2\ s^{-2}$, showing a strong turbulence layer there. This ~~turbulent~~ layer further moves to an upper altitude after 17:00 UTC.

The aerosol distribution varies along with the dynamical situation. The maximum aerosols concentration reaches 1800 cm^{-3} below 800 m at 12:00 and 1700 cm^{-3} below 1000 m ~~at 12:00 and~~ at 17:00 UTC~~ respectively~~. ~~Again, with so numerous aerosols~~As a result, the ~~cloud droplets concentration as a~~ domain mean CDNC has a maximum value of 900 *droplets* cm^{-3} at 12:00 UTC. This value decreases along time as more clouds dissipate. ~~At the break-up of~~After clouds start to break and become thinner, reduced cloud coverage allows more solar radiation to reach the ground. The maximum value of SWHR drastically changes from 45 $K\ day^{-1}$ at 12:00 UTC (almost compensating cloud top cooling) to about 10 $K\ day^{-1}$ at 16:00 UTC. The cloud top LW cooling is near constant at the end of convection phase with $-45\ K\ day^{-1}$.

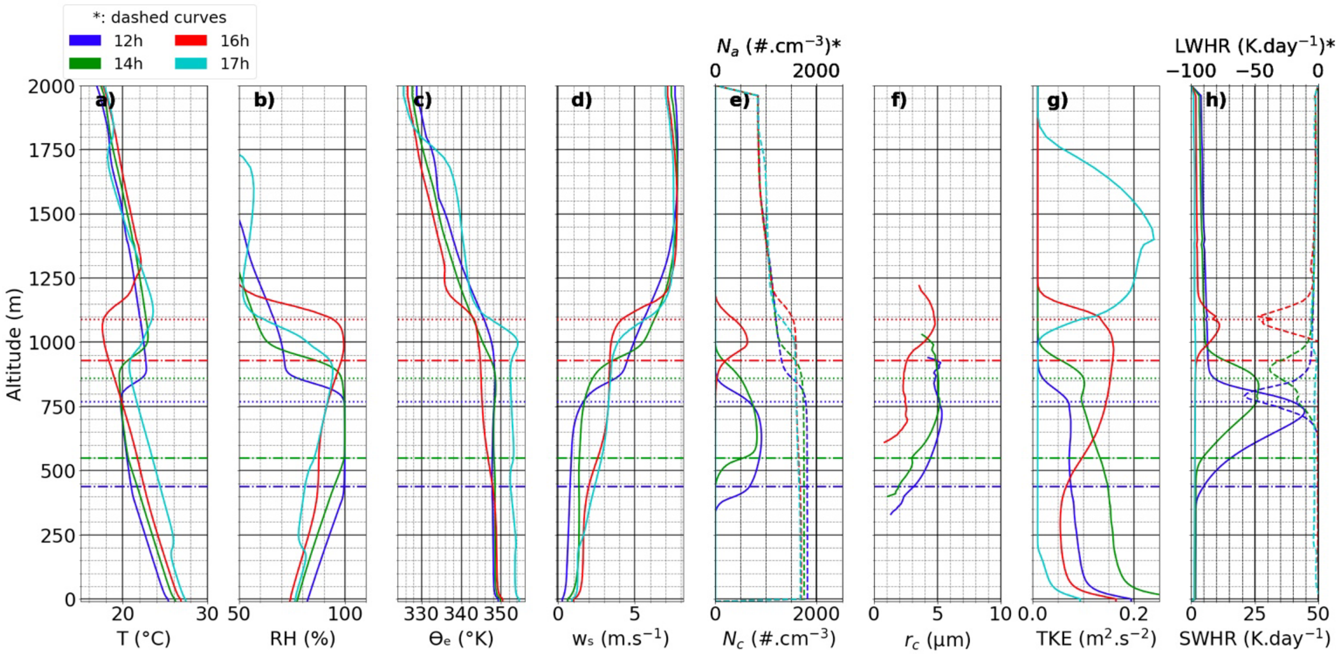

Figure 9. Profiles from left to right of temperature (T, a), relative humidity (RH, b), equivalent potential temperature (θ_e, c), horizontal wind speed (w_s, d), aerosol number concentration (N_a, dashed curve, e), cloud droplets number concentration (N_c,plain curve, e), cloud droplet radius (r_c, f), turbulent kinetic energy (TKE, g), longwave heating rate (LWHR, dashed curve, h) and shortwave heating rate (SWHR, plain curve, h) at 12:00, 14:00, 16:00 and 17:00 UTC. Dash-dot horizontal lines represent mean cloud base height (CBH) and dotted horizontal lines the mean cloud top height (CTH).

4. Sensitivity Study to Examine the Influence of Different Aerosol Profiles on LLSC ~~Diurnal~~ Life Cycle

Previous studies have indicated that the life cycle of stratus or stratocumulus within planetary boundary layer depends on the subtle balance among several critical while interconnected forcings including surface heat fluxes, cloud top and base radiative profiles, and thus turbulent mixing (*e.g.*, Stevens *et al*., 2005; Dussen *et al*., 2014, Ghonima *et al*., 2016). Apparently, our simulation results of the REF case support previous findings particularly for cases over land with surface sensible heat playing a significant role. Nevertheless, the role of aerosols in such a life cycle have rarely been ~~explored~~ examined in~~-~~ depth. Given the critical role of aerosols in determining cloud macro- and microphysical features and thus radiation, this is a ~~must-addressed~~critical issue to address in order to advance our understanding of the LLSC life cycle. A unique component of our study is the deployment of an interactive aerosol and atmospheric chemistry module in this observation-constrained modeling effort. In the following section we will discuss the ~~roles~~ likely impacts of aerosol variations in both number concentration and chemical composition ~~in influencing~~on the ~~diurnal~~ life cycle of observed LLSCs.

4.1 Aerosol profiles used in sensitivity simulations

The result of REF simulation has demonstrated that the Meso-NH model is able to reproduce many observed features of the July 3 LLSC case despite certain biases. Moreover, the dynamical, thermodynamic, and aerosol parameters are reasonably ~~well simulated~~captured by the model. ~~It is well acknowledged that~~To further reveal the impacts of aerosols~~,~~ from ~~both anthropogenic activities and biomass burning emissions, may influence cloud formation directly through absorbing solar radiation and indirectly by serving as CCN. To identify the aerosol~~ different emission sources ~~and~~ on the life cycle and key aerosol-cloud-radiation processes of modeled July 3 2023 LLSC case, ~~key processes of aerosol in such cloud enhancement, we tested the respective influence of anthropogenic sources and of aerosol semi-direct effects. For this purpose,~~ we have configured two ~~different~~ additional aerosol scenarios differing from the one used in REF run, based on observations during the field campaign (Figure A1 and Table 2), then applied them in a set of sensitivity simulations that would be otherwise the same as the configuration of REF simulation. Comparing to REF case, aerosol profile of POL has a slightly higher peak number concentration but in a different mode. In addition, sulfate mass ratio in POL aerosol profile is much higher than that of REF profile, while organic carbon mass ratios are quite close in both profiles.

Case		$N_a\ (cm^{-3})$	σ	D (nm)
POL	Mode 1	17100	1.54	55.19
	Mode 2	2650	2.14	101.83
CLEAN	Mode 1	65	1.49	63.98
	Mode 2	153	1.53	190.97

Table 2. Aerosol size distribution parameters for POL and CLEAN, ~~aerosols size distribution~~runs ~~described by~~including ~~two modes configured following three parameters (~~number concentration, standard deviation, and diameter~~)~~. For two aerosol modes.

To investigate the impacts of anthropogenic and biomass burning sources on cloud life cycle~~s~~, three additional numerical experiments were performed in addition to REF (Table 2)~~: (1)~~ The first is an experiment with aerosol profile that reflects an influence of ~~strong~~ heavy anthropogenic pollution ~~influence~~, obtained based on the aerosol chemical composition and size distribution observed by Brito *et* *al*. (2018) and Denjean *et al*. (2020a) ~~in~~ within urban plumes ~~originating~~ originated from ~~the polluted~~ cities of Lomé, Accra and Abidjan, ~~which is called~~hereafter referred as POL~~;~~. The second is~~(2)~~ an experiment designed using ~~to~~ a clean aerosol profile derived by ~~underestimate aerosol emission by~~ dividing REF aerosol concentration by 10, called CLEAN.~~;~~ The last one contains ~~and (3) an~~ three experiments without ~~(with)~~ aerosol semi-direct effect for CLEAN, POL, and REF aerosol profiles, respectively, called ADEOFF runs, which form paired simulations correspondingly with original CLEAN, POL, and REF runs, ~~(~~i.e., the ADEON~~)~~ runs of these scenarios.

4.2 Impact of aerosol loads on micro- and macrophysical properties of ~~low-level clouds~~LLSCs

~~Figure 10 compares three experiments conducted with enhanced anthropogenic emissions (POL), underestimated aerosol emissions (CLEAN) and background conditions (REF) to provide a quantitative estimation of aerosol loads on radiation and LLCs. In these simulations, both the semi-direct and the indirect effects are taken into account, which act simultaneously on cloud formation and evaporation. The POL case is mostly similar to REF.~~ Regarding the modeled macrophysical features, ~~Before the sunrise,~~ the domain mean CBH and CTH and ~~cloud presence probability~~cloud fraction of ~~both cases~~REF and POL are almost the same until 08:00 UTC (~~see~~ Figure 4 and A2 ~~and Figure A2a and A2b~~). After ~~this time~~sunrise, the ~~POL~~ mean CBH in POL is about 10 m ~~inferior to~~lower than that in REF, ~~the reference~~ reaching 340 m at 10:00 UTC, while the mean CTH is ~~mostly~~ only 10 m ~~superior~~ higher ~~even reaching~~at 940 m ~~instead of 920 m~~ at 15:00 UTC, indicating a slightly thinner cloud layer in POL than REF. The ~~cloud presence probabilities~~cloud fractions ~~of~~ in both cases are also largely the same until the extensive break-up occurs~~stage.~~ , when ~~For example,~~ the cloud ~~extend~~extent in POL displays an evident difference from that in REF, ~~s to~~i.e., 670 m thick (from 630 to 1300 m above the ground) at 16 UTC ~~instead~~ in POL versus ~~of~~ 540 m ~~as~~ in REF. On the other hand, POL and REF have produced clearly different cloud microphysical features including droplet number concentrations alongside mean radius throughout the lifetime of modeled clouds (Figure 10a and 10b). At the cloud formation (02:00 UTC), despite having similar liquid water content (LWC) around 0.35 $g\ m^{-3}$ at 250 m in both cases, N_c^{POL} reaches 333 *droplets* cm^{-3} and r_c^{POL} 6.45 μm instead of 653 *droplets* cm^{-3} and 5.1 μm for REF case~~. This is explained by the~~, indicating a result of differences mainly in ~~the characterization of~~ Mode 2 aerosol numbers ~~the aerosols~~ between the two scenarios (~~and the vertical wind speed as Abdul-Razzak and Ghan (2000) include vertical wind speed in their activation scheme. A~~at 02:00 UTC ~~this parameter~~the updraft near cloud base is rather weak at less than 0.30 $m\ s^{-1}$ ~~and allow~~in both cases) ~~POL and REF clouds droplets concentration and radius to evolve under this condition~~. This trend is reversed at 06:00 UTC when the ~~droplets number concentration~~CDNC and radius are equal to 1208 *droplets* cm^{-3} and 6.43 μm in~~for~~ POL, and 1305 *droplets* cm^{-3} and 6.12 μm ~~for~~ in REF, respectively. After 08 UTC and until the cloud break up, N_c^{POL} is superior to N_c^{REF} by reaching a maximum difference of 1425 *droplets* cm^{-3} at 14:00 UTC. Their respective radii are 4.42 μm and 5.18 μm while the liquid water content profiles are quite the same as near 0.47 $g\ m^{-3}$ at 750 m. The difference between POL and REF in CDNC after sunrise suggests that the activation favors the POL profile with higher sulfate content when updraft is strengthened. These results are in good agreement with the ACPIM parcel model simulation done by Taylor *et al*. (2019) where CDNC varies in a range of 500−1400 *droplets* cm^{-3} depending on the inland or offshore (offshore + local emissions) aerosols origin.

The difference between CLEAN and REF in cloud macrophysical features such as CBH and CTH ~~between CLEAN and REF~~ is visible though largely limited to a few tens of meters. However, their differences in ~~other macrophysical features including~~ cloud ~~coverage~~ fraction and microphysical features are rather significant. ~~Indeed~~As expected, from formation to break-up of ~~stratiform~~ the clouds, N_c^{CLEAN} is ~~inferior to~~lower than N_c^{REF} and r_c^{CLEAN} is ~~superior to~~larger than r_c^{REF}. At 02:00 UTC, N_c^{CLEAN} has a maximum value of 181 $droplets\ cm^{-3}$ ~~for a radius~~and r_c^{CLEAN} of 7.58 μm, in comparison to ~~instead of~~ 653 $droplets\ cm^{-3}$ and 5.1 μm for N_c^{REF} and r_c^{REF} respectively with the same liquid water content value (0.35 $g\ m^{-3}$). ~~Between 02:00 UTC and 08:00 UTC,~~ r_c^{CLEAN} further increases to ~~reach at the latter time~~ 12.55 μm at 08:00 UTC, ~~. After 08:00 UTC,~~ ~~r_c^{CLEAN}~~then decreases slowly ~~showing~~ to a maximum value of 10.97 μm at 14:00 UTC~~. It has to be notified for this time that~~ with LWC^{CLEAN} reaches near 0.45 $g\ m^{-3}$ instead of 0.49 $g\ m^{-3}$ for LWC^{REF}, ~~. This change in the available volume of liquid water with such droplet size explains the decreasing of~~ ~~N_c^{CLEAN}~~ ~~while the aerosol number concentration remains stable around 200-250~~ ~~cm^{-3}~~likely due to an increased activation ratio of aerosols after sunrise. Despite a relatively larger droplet size in CLEAN than POL and REF case, there is no clear sign of massive formation of drizzles even during the convection stage (Fig. 10). Nevertheless, sedimentation thus evaporation of larger droplets from entrainment zone and cloud base could likely create a thermodynamic perturbation (*e.g.*, Stevens *et al*., 1998; Jiang *et al*., 2002). In a LES simulations using passive aerosol profile for July 4-5 DACCIWA case, Dearden *et al.* (2018) found that the sedimentation would remove droplets from the entrainment zone thus, through a feedback, lead to a cloud deck with higher LWP while smaller CF than the case where sedimentation is completely excluded. This could imply a similar contrast between CLEAN and the two polluted cases in our simulations, by simply assuming the total sedimentation amount is proportional to the droplet size (*i.e*., inversely to the CDNC), though the quantity of such a perturbation seems rather small here, not to mention the more sophisticated feedback involved in our case introduced by the dynamic aerosol-cloud interaction in our model.

As demonstrated from above discussions that modeled cloud microphysical features respond to the variation of aerosol number concentration as expected, *i.e.*, higher aerosol concentration leads to higher cloud droplet number concentration (POL > REF > CLEAN) while smaller mean droplet radius (POL < REF < CLEAN) and hence a higher cloud reflectivity (POL > REF > CLEAN). Though exception does exist. For example, differences in the aerosol size distribution and chemical composition between REF and POL could lead to an outcome opposite to the general expectation particularly under a weak dynamical condition. ~~However, interestingly, as~~As shown in Fig. 10c, the response of the incoming solar radiation ~~(SWRADSURF)~~ at ground (SWRADSURF) does not always follow ~~always~~ such an expectation in cloud microphysics and thus reflectivity in responding to aerosol variation. In fact, SWRADSURF appears to be higher in POL than REF from sunrise to 13:00 UTC, and the values in both runs are also clearly higher than that in CLEAN. This tendency is only reversed after 13:00 UTC when solar flux reaches its peak until the break-up stage.

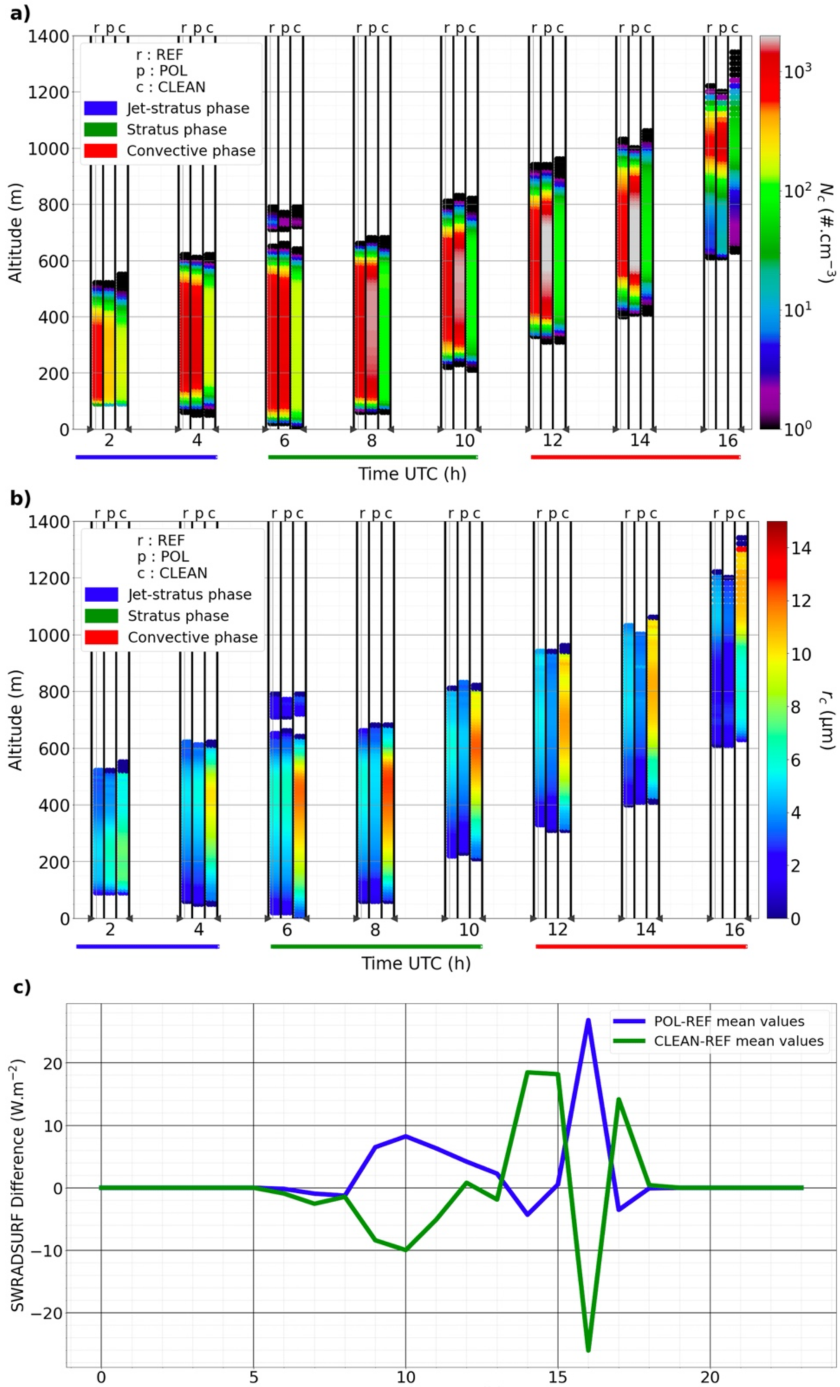

Figure 10. Evolution of cloud droplets concentration N_c (top) and cloud droplets radius r_c (middle) with the scenarios given and designated by letter a (REF), b (POL) and c (CLEAN). Bottom panel gives the evolution of mean domain SWRADSURF differences between POL / CLEAN and REF.

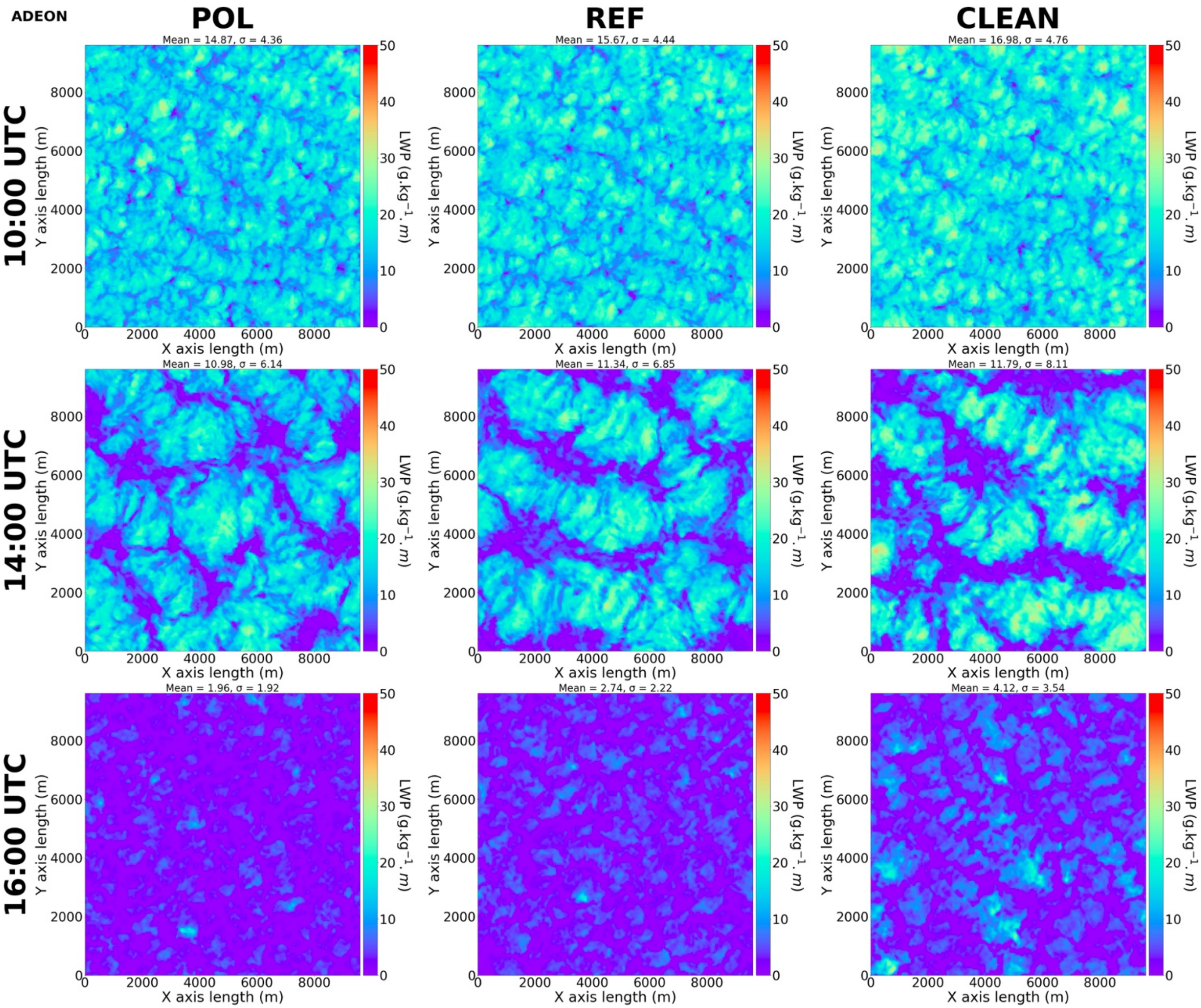

Figure 11. Liquid water path (LWP, $g\ kg^{-1}\ m$) in POL (left column), REF (mid-column), and CLEAN (right column) runs at 10:00 UTC (top row), 14:00 UTC (middle row), and 16:00 UTC (bottom row).

Figure 11 shows that the major reason behind the above-described trend of SWRADSURF is the difference in cloud ~~coverage~~ fraction in competing with the effect brought by different cloud reflectivity of various runs, especially before noon when zenith angle is still high. After sunrise, the cloud top starts to rise and cloud layer becomes thicker. In the meantime, this upward development brings a downward entrainment of dry air from the temperature inversion zone above the cloud top and causes evaporation in the cloud. For a cloud with a large quantity of very small droplets as in POL and REF, the evaporation rate of droplets would exceed that in CLEAN case, thus more cloud-void spaces or a thinner cloud layer would form much easier than in the latter case. Note that a similar macrophysical response to aerosol concentration variation (in a simple high versus low setting) was also suggested in a marine cloud case though with a coarse vertical resolution of 50 m (Wang *et al*., 2003). As shown in Fig. 11 and Table 3, cloud layer in CLEAN is slightly denser than those in POL and REF while cloud-void or thin cloud pixels account for a substantially lower ratio within the domain. Thus, before noontime, cloud reflectivity seems to become the secondary factor comparing to ~~the cloud-void space~~cloud fraction in determining the value of SWRADSURF. As a result, SWRADSURF in CLEAN is significantly lower than REF then POL until zenith angle becomes lower closer to noontime. The lower SWRADSURF in CLEAN would also have reduced the turbulent mixing as well as delayed the convection that would cause extensive cloud break-up. At 14:00 UTC, difference in cloud thickness and cloud-void space still exists ~~while~~ but becomes relatively smaller among the three different runs (Fig. 11 and Table 3), cloud reflectivity now becomes the primary reason to cause a different SWRADSURF as shown in Fig. 10 (bottom panel). Interestingly, modeled clouds in POL and REF appear to dissipate earlier and much faster than in CLEAN in the break-up stage (Fig. 11, bottom panel).

	LWP 10 UTC	PCP 10 UTC	LWP 14 UTC	PCP 14 UTC	LWP 16 UTC	~~PRP~~ PCP 16 UTC
POL	14.87	12.79	10.98	42.17	1.96	99.66
REF	15.67	10.11	11.34	42.69	2.74	99.67
CLEAN	16.98	6.95	11.79	44.93	4.12	94.47

Table 3. Domain averaged liquid water path (LWP; $g\ kg^{-1}\ m$) and poor-cloud pixel percentage (PCP, defined by the percentage of pixels where LWP < 10 $g\ kg^{-1}\ m$; percentage) in three different runs.

Looking into various timely varying metrics of LWP in different model runs, we find that in general, LWP is inversely promotional to CDNC, as LWP in POL < LWP in REF < LWP in CLEAN, and this is applied to different metrics of LWP (Fig. 12, Table 3). However, in comparison, the peak LWP varies less significantly in CLEAN case, while peak LWPs in two other runs decrease with domain averaged quantities in convection stage. There were different opinions regarding the mechanisms behind such an inverse relation between LWP and CDNC (*e.g.*, Ackerman *et al*., 2004; Bretherton *et al*., 2007), not to mention that most such hypotheses were proposed based on the cases of marine low clouds that might not be directly applied to the cases over land. In our analysis, the difference in turbulent mixing driven by the surface radiative heating, as influenced by different microphysical features in various cases, seems having played a critical role. The situation of cloud fraction (CF) is somewhat more complicated. As shown in Table 3 and Fig. A4, CF relation with CDNC varies in different stages. An inverse relation between CF and CDNC generally stands in the earlier and later period of the convection stage, in the middle of the convection stage (13:00-15:00 UTC), the above relation, however, would reverse, alongside the vertical cloud extent as discussed previously.

To summarize, as expected, aerosol concentration is a major factor in controlling the cloud microphysical features by ~~changing~~ determining the simulated droplet number concentration and radius ~~for~~ of clouds with similar liquid water content. However, our results suggest that cloud reflectivity as a function of CDNC is not necessarily a dominant factor to solely determine the surface incoming solar radiation particularly when dynamical situation is more complicated to maintain a constant LWC. Instead, the response of ~~despite this well-known Twomey effect the incoming solar radiation at ground did not decrease due to additional CDNC. Instead,~~ cloud macrophysical features ~~and in particular~~ such as cloud-void space (or inversely, cloud fraction) as well as LWP to the variation caused by dry entrainment from inversion~~e~~ layer above the cloud is the dominant factor ~~impacting~~ in determining the incoming solar radiation at ground. ~~Cloud macrophysical properties determine the break-up speed of modeled clouds and therefore, the life cycle of the modeled LLSCs.~~ Our study weights in both size distribution and chemical composition in aerosol variation for modeling such situations, the results indicate a critical role of cloud microphysical response to aerosol in deciding the LWP and CF response. The overall negative response of LWP to aerosol concentration derived here agrees with several previous studies (*e.g.*, Ackerman *et al*., 2004; Jiang and Feingold, 2006). While the case for CF response is more complicated, varying in different stages in cloud life cycle. It is worth indicating though, another factor that might contribute to the cloud life cycle, *i.e.*, the atmospheric heating caused by the semi-direct ~~optical~~ effect of absorbing aerosol component such as black carbon has not been analyzed up to this moment and will be discussed in the following section.

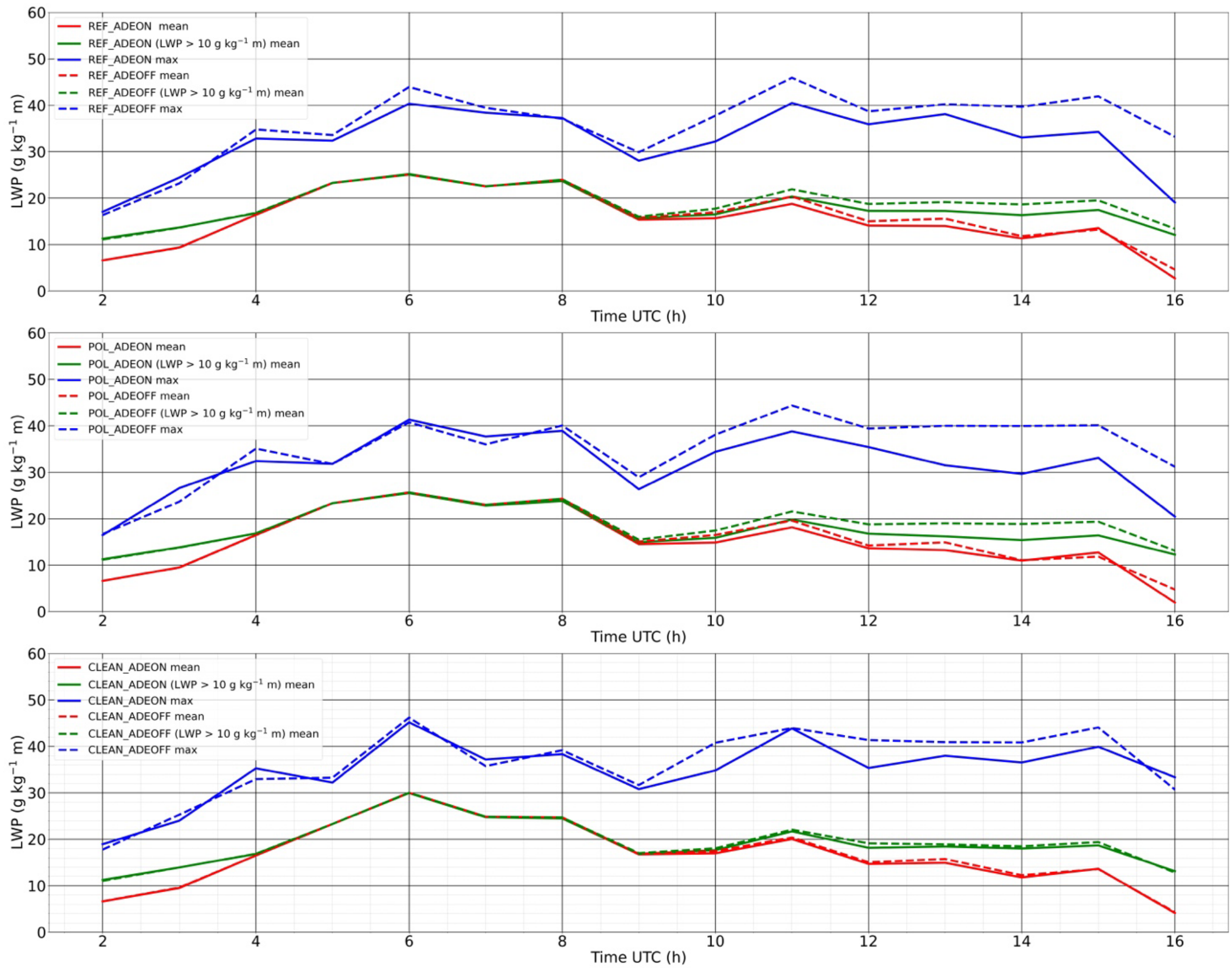

Figure 12. Domain averaged LWP (LWP mean), maximum LWP (LWP max), and domain averaged LWP over pixels where LWP > 10 $g\ kg^{-1}\ m$ in AODON and AODOFF runs in REF (upper panel), POL (middle panel), and CLEAN (lower panel) cases, derived using hourly model outputs.

4.3 Impact of aerosol semi-direct effect on ~~low-level cloud~~LLSCs

The semi-direct effect of aerosols resulted from SW radiation absorption by absorbing aerosol, could affect ~~on LLSCs that represents the modifications of the~~ atmospheric dynamics surrounding LLSCs ~~properties and~~and thus their life cycle. ~~atmospheric dynamics due to absorption of SW radiation by absorbing aerosol.~~ This effect has been ~~estimated~~ examined ~~here~~ in our study by ~~conducting~~ comparing the results of three additional experiments, constructed accordingly in the same way as their original experiments (hereafter ADEON ~~including~~ of REF, POL, and CLEAN) but excluding aerosol direct effects (named ADEOFF), ~~and then comparing the results between each~~with those of the three paired original runs. Apparently, BC is the major species behind the semi-direct effect in our case~~ study~~.

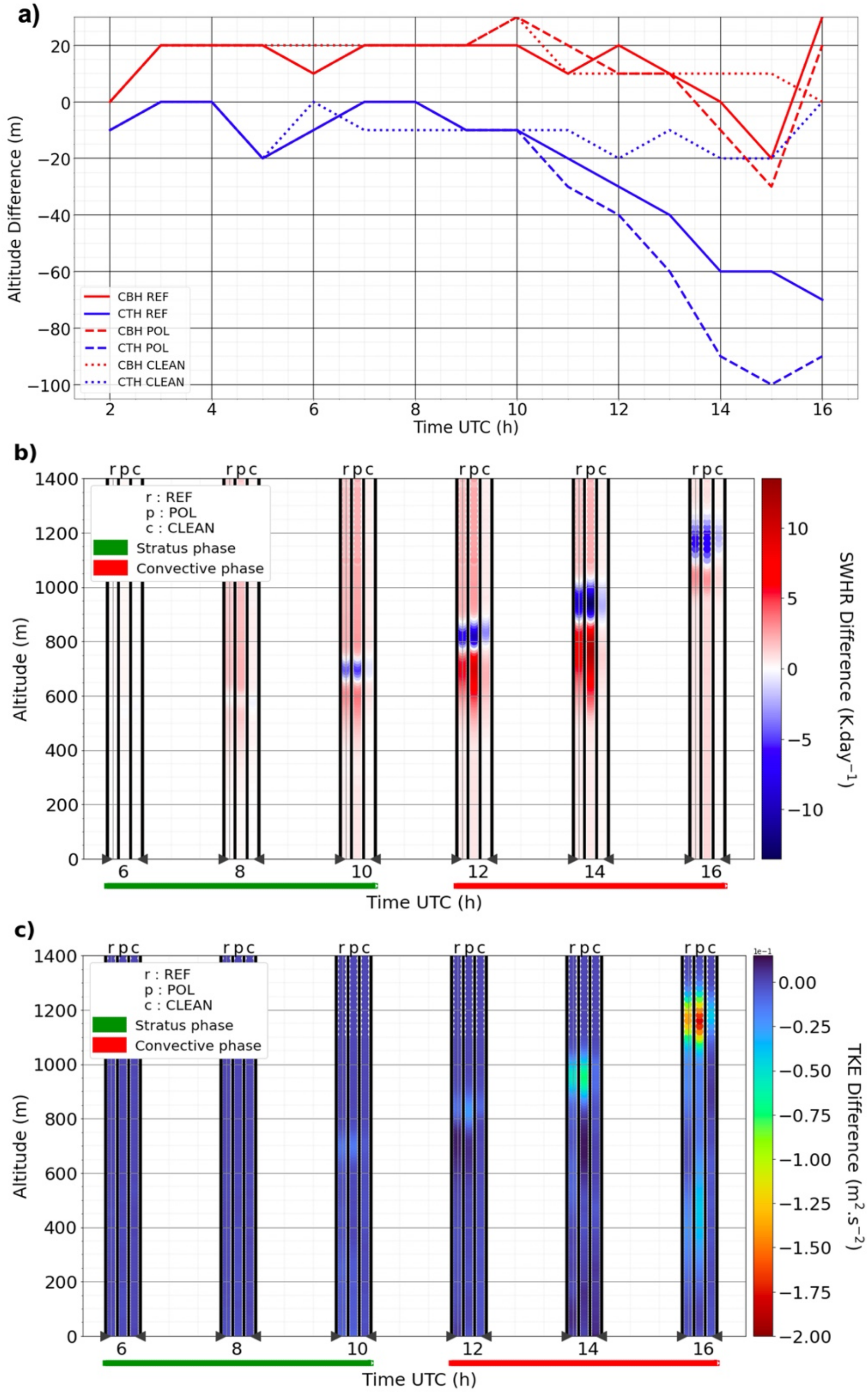
a)
Altitude Difference (m)
Time UTC (h)
CBH REF
CTH REF
CBH POL
CTH POL
CBH CLEAN
CTH CLEAN
b)
r p c
r : REF
p : POL
c : CLEAN
Stratus phase
Convective phase
Altitude (m)
Time UTC (h)
SWHR Difference (K.day^{-1})
c)
r p c
r : REF
p : POL
c : CLEAN
Stratus phase
Convective phase
Altitude (m)
Time UTC (h)
TKE Difference (m^2.s^{-2})

Figure 13~~2~~. Evolution of the difference of the mean CBH and CTH (a), SWHR (b) and TKE (c) between the simulation runs with and without aerosol direct effect (ADEON-ADEOFF) for REF, POL and CLEAN.

The changes in cloud top and base, SWHR, and TKE due to aerosol absorption and ~~potential~~ associated feedbacks are shown in Figure ~~12~~13. The results demonstrate that light-absorbing BC aerosols can cause a substantial atmospheric heating accompanied by a ~~substantial~~ warming tendency near the top of LLSCs ~~top~~ (Figure ~~12b~~13b). At 14:00 UTC, t~~T~~he domain averaged heating due to BC aerosols (difference in SWHR ~~difference~~between AODON and AODOFF) and a consequent cooling just above the cloud due mostly to the cloud top change are ~~in CLEAN case is rather insignificant in comparison with the two other cases as 1.30 K day^{-1} (and a cooling −2.25 K day^{-1} above due to cloud top change) at 14:00 UTC, whereas it reaches~~ 12.16 K day^{-1} and ~~(~~−13.14 K day^{-1}~~)~~ ~~for~~ in POL, and 7.71 K day^{-1} and ~~(~~−9.24 K day^{-1}~~)~~ in REF, respectively. In comparison, the atmospheric heating and associated cooling of 1.30 K day^{-1} and −2.25 K day^{-1} in CLEAN case are clearly insignificant. Accordingly, in ADEON runs, more water vapor tends to condense onto cloud droplets under the higher relative humidity in the lower PBL and decreasing turbulent mixing (Figure ~~12c~~13c, with a maximum decreasing of −0.18 m^2 s^{-2} for POL), leading to a decrease of the cloud top height, limiting entrainment, and also reducing~~ed~~ ~~SW reflection~~incoming solar radiation at surface due to BC in-cloud absorption. The cloud top height reduction due to the semi-direct effect in two polluted cases POL and REF is quite ~~significant~~ substantial as shown in Figure ~~12a~~13a, where CTH in POL and REF has decreased by up to 100 and 70 meters due to the presence of BC, respectively. On the other hand, CBH is also increased about 20 meters in both cases before break-up, suggesting a thinner cloud layer owing to the semi-direct effect. In comparison, CTH, ~~and~~ CBH, and thus cloud vertical extent appears to be less affected in CLEAN run due to its low BC content. Before break-up, in-cloud TKE below the heating layer has been reduced in some extent (Fig.~~12c~~13c). On the other hand, due to a lower cloud top in the polluted cases, planetary boundary layer ~~top~~ height ~~with active turbulent exchange~~ would also be lowered. The effect of BC absorption in lowering modeled cloud top and thinning cloud layer ~~s~~ in POL and REF (implying a reduced upward development) is likely another factor to slow down their break-up as discussed before.

The impact of the semi-direct effect on other critical macrophysical features such as cloud fraction and LWP can be also seen from the model results. For instance, LWP particularly the maximum LWP is clearly lower in the AODON runs of the two polluted cases (REF and POL) (Fig. 12). In addition, an increase of cloud fraction due to the semi-direct effect can be seen throughout the convection stage until 15:00 UTC when massive cloud break-up occurs (Fig. A4). All these imply a critical role of the semi-direct effect on cloud radiation.

We find that the semi-direct effect can ~~manifest~~ both ~~an enhancing~~ enhance and ~~a~~ weaken~~ing~~ ~~contribution to~~ the (negative) indirect radiative forcing as also indicated by some previous works (Lohmann and Feichter, 2001; Koch and Del Genio, 2010a; Huang *et al*., 2014; Yamaguchi *et al*., 2015; Stjern *et al*., 2017; Kreidenweis *et al*., 2019). ~~At 14:00 UTC~~In the convection stage before 15:00 UTC, the ~~flux~~ difference in SWRADSURF between ADEON and ADEOFF ~~at ground~~ is negative, reaching~~es~~ −33 $W\ m^{-2}$ and −75 $W\ m^{-2}$ for REF and POL at 14:00 UTC, respectively (Fig. ~~13c~~14c). This can be~~is~~ explained by ~~a decreased void space~~an increase in cloud fraction in ADEON runs (Fig. A4, Table 3) that allows less solar irradiance to attain the surface despite the cloud layer being thinner, not to mention that solar irradiance itself has already been reduced due to BC absorption (Fig. 12, ~~13c~~ 14c and A3).~~,~~ Note that the different chemical compositions between POL and REF also lead to a quantitatively different effect. ~~hence~~ Hence, the semi-direct effect contributes positively to the enhancement of (negative) indirect radiative forcing in this case. ~~But~~ On the other hand, at 16:00 UTC, the flux difference between ADEON and ADEOFF becomes positive with values for REF and POL as 32 $W\ m^{-2}$ and 66 $W\ m^{-2}$, respectively. As the clouds break up more slowly~~er~~ in ADEOFF during this stage due to ~~being~~ thicker cloud layers (Fig. A3 and A4), more clouds inside the domain with increased thickness causes weaker SW irradiance reaching the ground. In other words, the semi-direct effect makes the cloud dissipate faster in the convective stage. In this case, the semi-direct effect weakens the semidirect radiative forcing.

The above results have demonstrated the important role of solar absorption by aerosols in determining the life cycle of LLSCs. The atmospheric heating by light absorbing BC would limit the elevation of cloud top, especially during the break-up stage (Koch and Del Genio, 2010b; Zhang and Zuidema, 2019). Such a heating can also ~~decrease cloud-void space~~increase cloud fraction then delay break-up until late afternoon, especially for clouds with higher cloud droplet number concentration in polluted environment such as in POL and REF runs (opposite to the outcome by considering aerosol number concentration only), and thus affect the indirect effect of aerosols. ~~This study case also exhibits either a positive (e.g., decreasing cloud-void space) or a negative (e.g., accelerating break-up in late afternoon due to a thinner cloud) contribution of the semi-direct effect to the indirect radiative forcing.~~Note that our modeling configurations are based on the aerosol profiles that are relatively well-mixed throughout the PBL then with concentration gradually decreasing along altitude above PBL. Certain previous sensitivity experiments suggested that the location of BC layer within or above PBL could have different impacts on the development of convection, entrainment, and thus life cycle of the low clouds within PBL. For instance, Johnson *et al*. (2004) suggested that without considering the indirect effect of aerosols, BC existing within boundary layer would lower LWP by nearly 20% in a marine low stratocumulus case, where the cloud response is less sensitive to the surface shortwave heating change comparing to the situation in our case. Feingold *et al*. (2005) found that smoke plumes containing BC near the surface would reduce the cloudiness through both the atmospheric heating and weakening effect on surface heat fluxes by BC. These results though obtained with somewhat different model configurations than ours (e.g., coarser vertical resolution, different surface, etc.) are in a qualitative agreement with our findings. Nevertheless, the unique configuration of our model allows us to quantitatively examine the semi-direct effect with varying aerosol chemical compositions and thus extent of aerosol absorption. This has led us to reveal further insights of the complicated interplays among various aerosol effects besides their individual impacts on the life cycle of LLSCs.

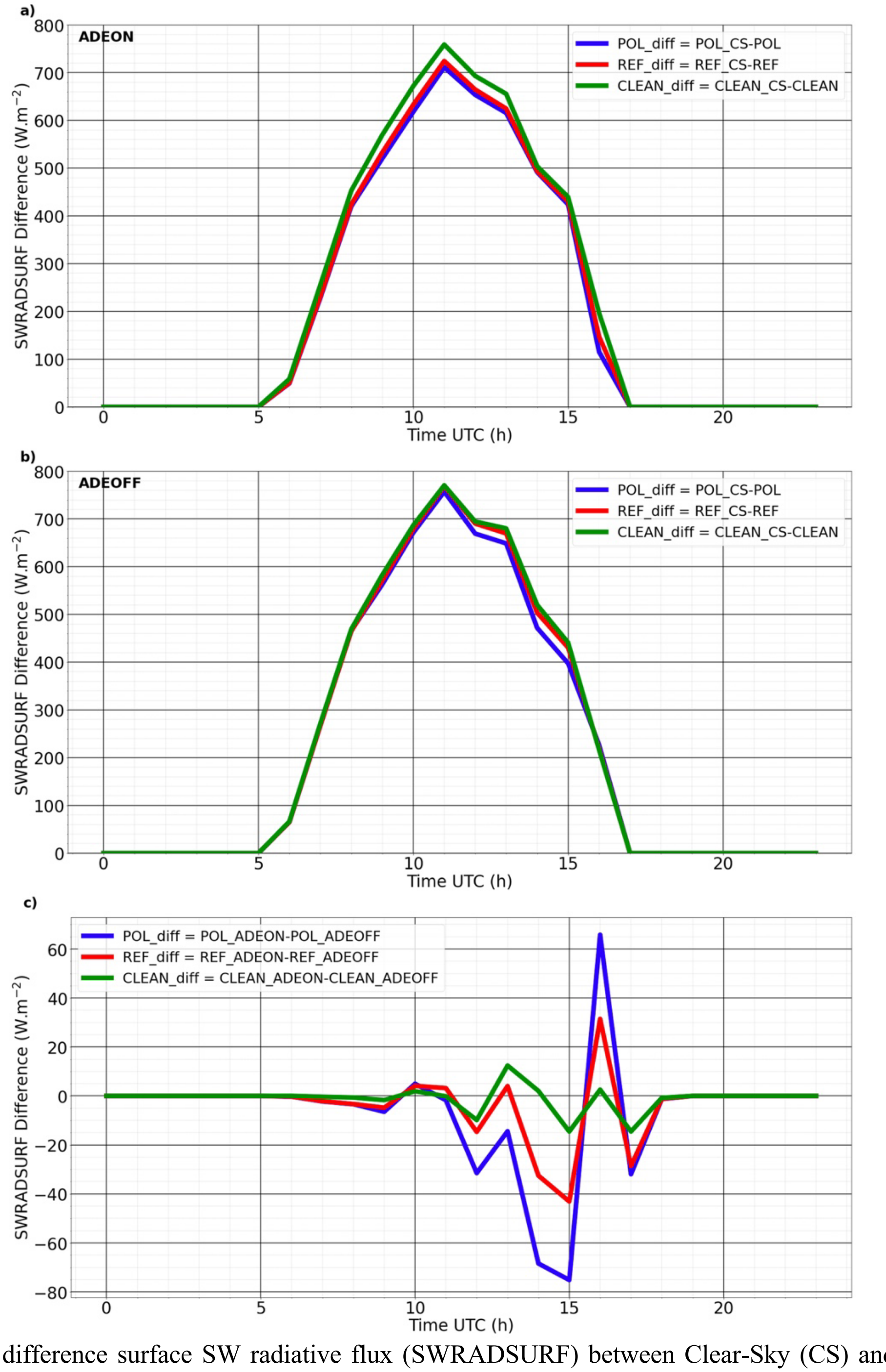

Figure ~~13~~14. Mean difference surface SW radiative flux (SWRADSURF) between Clear-Sky (CS) and cloudy scenarios giving the flux dissipated by clouds in ADEON (a) and ADEOFF (b) configurations. SWRADSURF difference between ADEON and ADEOFF configuration for the three scenarios (c).

5. Conclusions

A characteristic case of the LLSCs over ~~SWA~~ southern West Africa has been simulated with Meso-NH model in ~~high-resolution~~a Large-Eddy Simulation configuration constrained by ~~DACCIWA~~ the measurements from the DACCIWA field campaign. The model has successfully reproduced the observed nocturnal-to-diurnal life cycle alongside key macro- and microphysical features as well as surface radiative and heat fluxes. To determine the impact of aerosols on the ~~LLSCs diurnal~~ modeled life cycle of LLSCs, sensitivity simulations using several different aerosol profiles have also been conducted. These aerosol profiles contain different ~~number concentrations~~size distributions and chemical compositions~~, in order to~~ reflecting the situations associated with various aerosol populations encountered during the field campaign.

The results from various sensitivity simulations suggest that both aerosol ~~concentration~~ size distribution and chemical composition can effectively influence the LLSCs life cycle. The impact of the aerosol ~~concentration~~size distribution, as reflected from a comparison among simulations using aerosol profiles with different number concentrations and modal distributions, is initiated from resultant cloud microphysical features in particular the cloud droplet number concentration and mean droplet size. Such a difference created by different aerosol ~~number concentration~~size distributions also affect cloud reflectivity as expected. Interestingly, we have found that the difference in cloud reflectivity caused by different aerosol concentration does not always dominate the surface incoming solar radiation and thus cloud development after sunrise. This is due to ~~another~~ a competing factor: the ~~cloud-void space~~cloud fraction caused by the air entrained from the inversion layer above cloud top and associated evaporation of cloud droplets as a function of CDNC, which specifically dominates the variation of surface incoming solar radiation before noontime. Clouds influenced by higher aerosol concentrations and thus having higher ~~cloud droplet~~ number concentration and smaller ~~droplet~~ sizes of cloud droplets are found to evaporate more easily and thus impose ~~more cloud-void spaces~~a lower cloud fraction. For the same reason, clouds with higher droplet concentration are likely to break up earlier.

In addition, our sensitivity runs including versus excluding aerosol direct radiative effects have also demonstrated the ~~im- pact~~impact specifically of solar absorption by black carbon on the cloud life cycle. The excessive atmospheric heating ~~by black carbon~~ reaching 12 $K\ day^{-1}$ introduced by black carbon in our modeled cases is found to be able to lower the cloud top height as well as liquid water path, ~~and~~ reduce dry entrainment, and increase cloud fraction. Working with the ~~above-indicated aerosol concentration effect~~cloud fraction response to aerosol size distribution, this heating and its consequences might delay break-up of the LLSCs until late afternoon.~~,~~ W~~w~~hile beyond that point, the modeled clouds in polluted cases with higher aerosol concentrations and BC included would break up faster due to their thinner cloud layers. Therefore, the semi-direct effect can contribute positively to the indirect radiative forcing (negative in quantity) ~~due to~~by ~~decreased cloud-void space~~increasing cloud fraction, or negatively by causing thinner cloud layer and thus a faster cloud break-up in late afternoon, all depending on the phase in stratiform cloud ~~diurnal~~ life cycle as demonstrated in this study and several previous ones.

Our study has demonstrated that the life cycle and thus the radiative forcing of LLSCs over land area of SWA can be substantially influenced by aerosols from both long-range transported biomass burning plumes and from local ~~urban~~ anthropogenic emissions. In fact, more aerosol profiles had been collected during the DACCIWA campaign besides the ones used in this study. Future research works could reveal the aerosol impact under an even broader range of aerosol properties and to examine the temporal variations of LLSCs radiative effects ~~evolved~~ evolving with different large-scale meteorological conditions with different associated airmass. More analysis on different cloud cases in SWA would also be able to assess or refute current results on semi-direct effect.

Code and data availability. The data obtained during the DACCIWA campaign at the Savè supersite alongside all other data used in this study are publicly available on the SEDOO database (http://baobab.sedoo.fr/DACCIWA/). The Meso-NH code is maintained and updated by LAERO and CNRM, it is freely available for download at http://mesonh.aero.obs-mip.fr/mesonh52/.

Author contributions. LD and CW designed the simulations and LD conducted model simulations and data analyses. LD and CW wrote this paper with contribution from all co-authors. CW advised and helped to better understand the different aspects of this research work. PT advised and trained LD for Meso-NH and ORILAM module use. CD processed and provided the aerosol profiles used in previous simulations and NM was part of this work. MZ helped to select the study case and advised during the study case construction and analysis. AD brought a critical eye to this work.

Competing interests. The authors declare that they have no conflict of interest.

Acknowledgements. This study is supported by L'Agence National de la Recherche (ANR) of France under "Programme d'Investissements d'Avenir" (ANR-18-MPGA-003 EUROACE) and co-funded by University Toulouse III Paul Sabatier. The computation of this work was performed using HPC resources of French GENCI-IDRIS (Grant A0110110967 and A0090110967) and French Regional Computations center CALMIP. LD thanks the Laboratoire d'Aérologie, Université de Toulouse, France, for funding and hosting his Ph.D. research activities. LD also thanks the MesoNH team, especially Quentin Rodier, Juan Escobar, and Philippe Wautelet, for their advises on using Meso-NH, Benoit Vié and Marie Mazoyer for their help to handle and modify microphysical scheme LIMA, Quentin Libois for explaining the details of Meso-NH's radiative schemes, and specifically Fabienne Lohou (LAERO) for her introduction of DACCIWA campaign alongside her guidance in using relevant data products. A special thanks the authors to all people whose work was involved in the measurement and processing of DACCIWA campaign data especially over the Savè supersite. Many constructive comments and suggestions from Dr. Mónica Zamora Zapata and an anonymous reviewer as well as the handling editor, Dr. Graham Feingold have made a substantial impact on our effort to improve the quality of the manuscript.

Appendix A

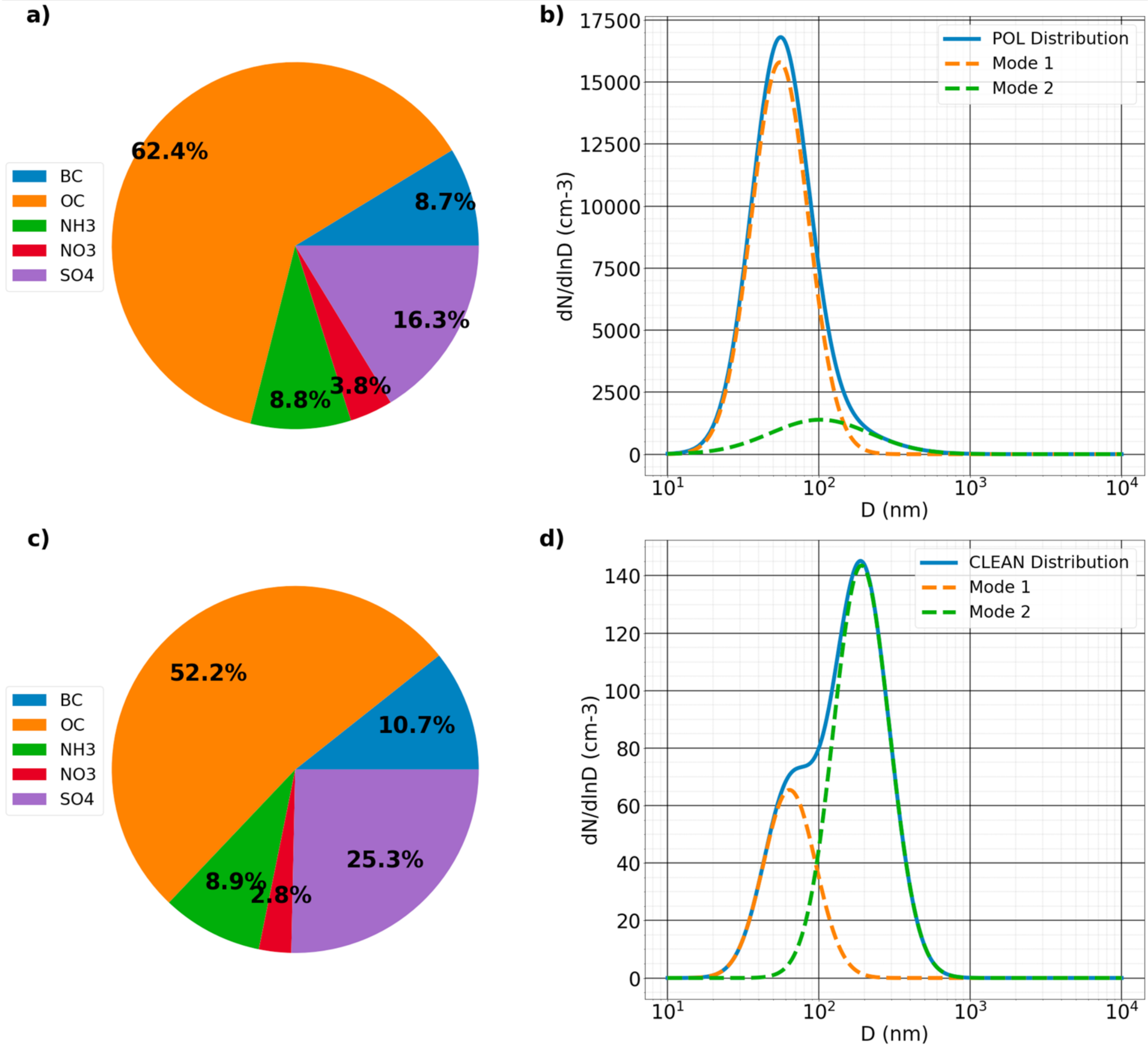

Figure A1. Mass composition (a,c) and size distribution provided by (Denjean et al., 2020a) and fitted into 2 modes described in Table 2 (b,d) for scenarios POL (top), CLEAN (bottom).

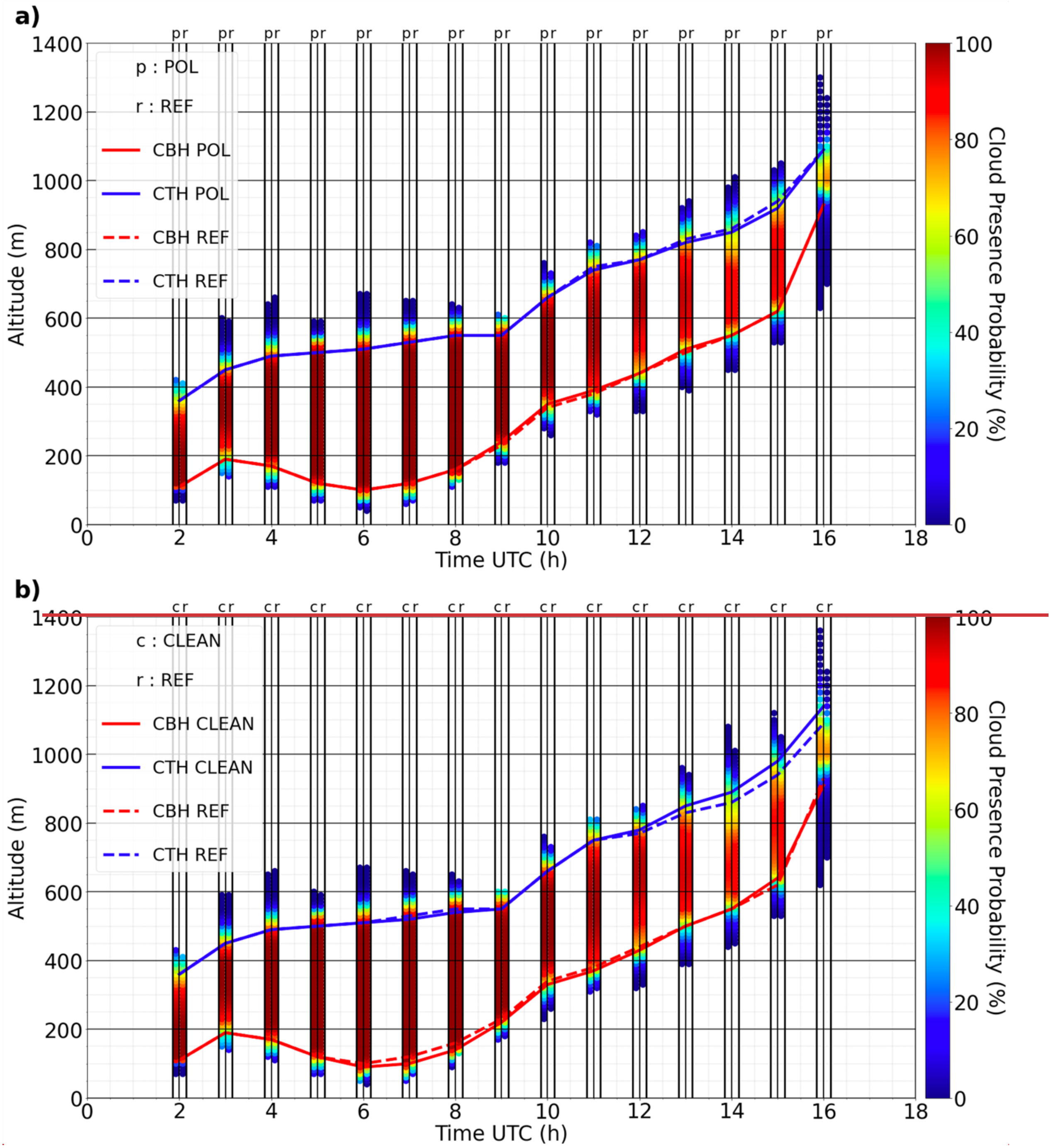

a)
p : POL
r : REF
CBH POL
CTH POL
CBH REF
CTH REF
Altitude (m)
Time UTC (h)
Cloud Presence Probability (%)
b)
c : CLEAN
r : REF
CBH CLEAN
CTH CLEAN
CBH REF
CTH REF
Altitude (m)
Time UTC (h)
Cloud Presence Probability (%)

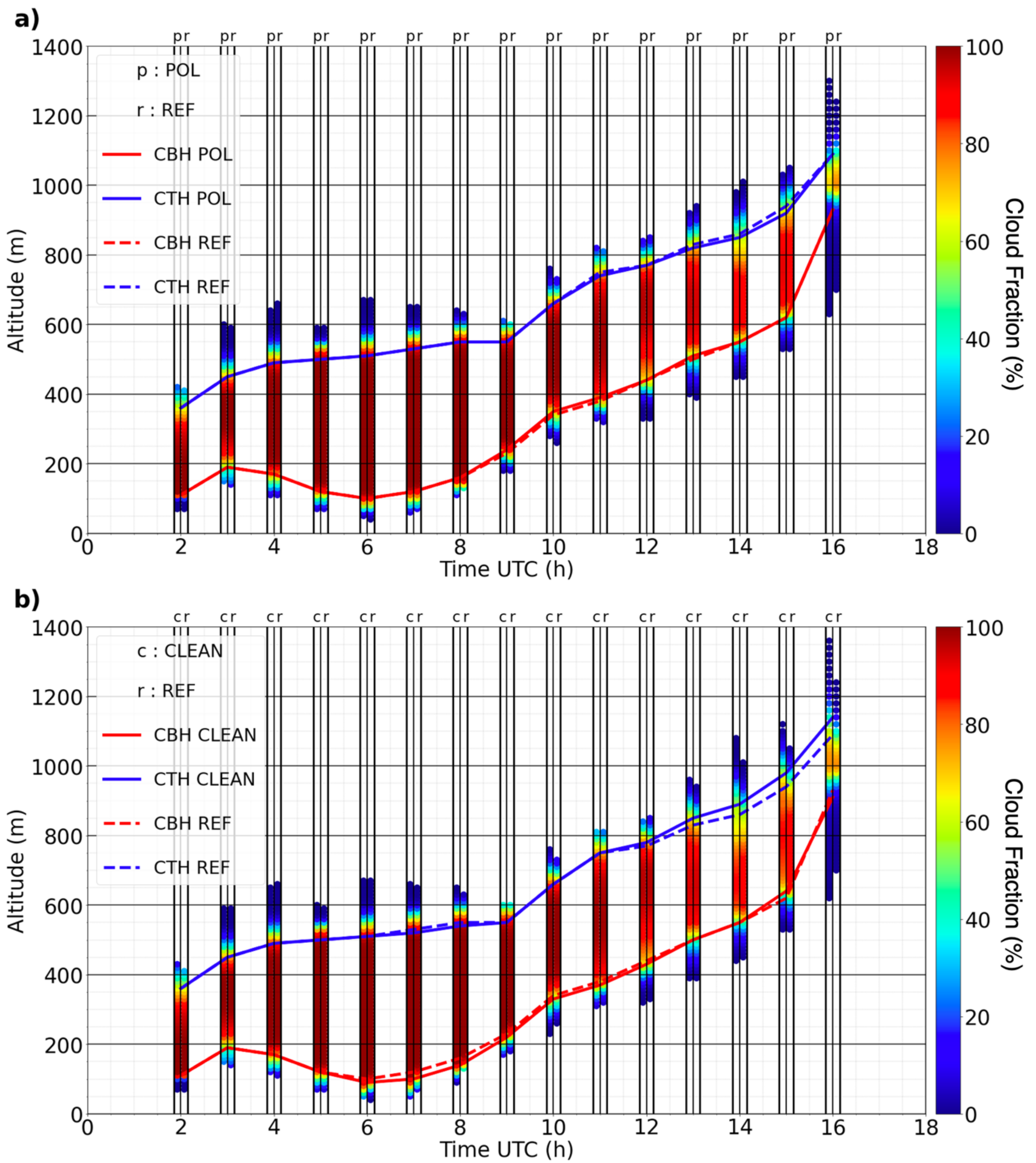

Figure A2. Mean LLSCs deck evolution of POL (a) and CLEAN (b) cases with the representation of REF's one to make comparison and REF_NOBC ADEON and ADEOFF runs (c), vertical color bars for POL/CLEAN (left) and REF (right) attribute at each altitude level a cloud presence density for both cases at each hour.

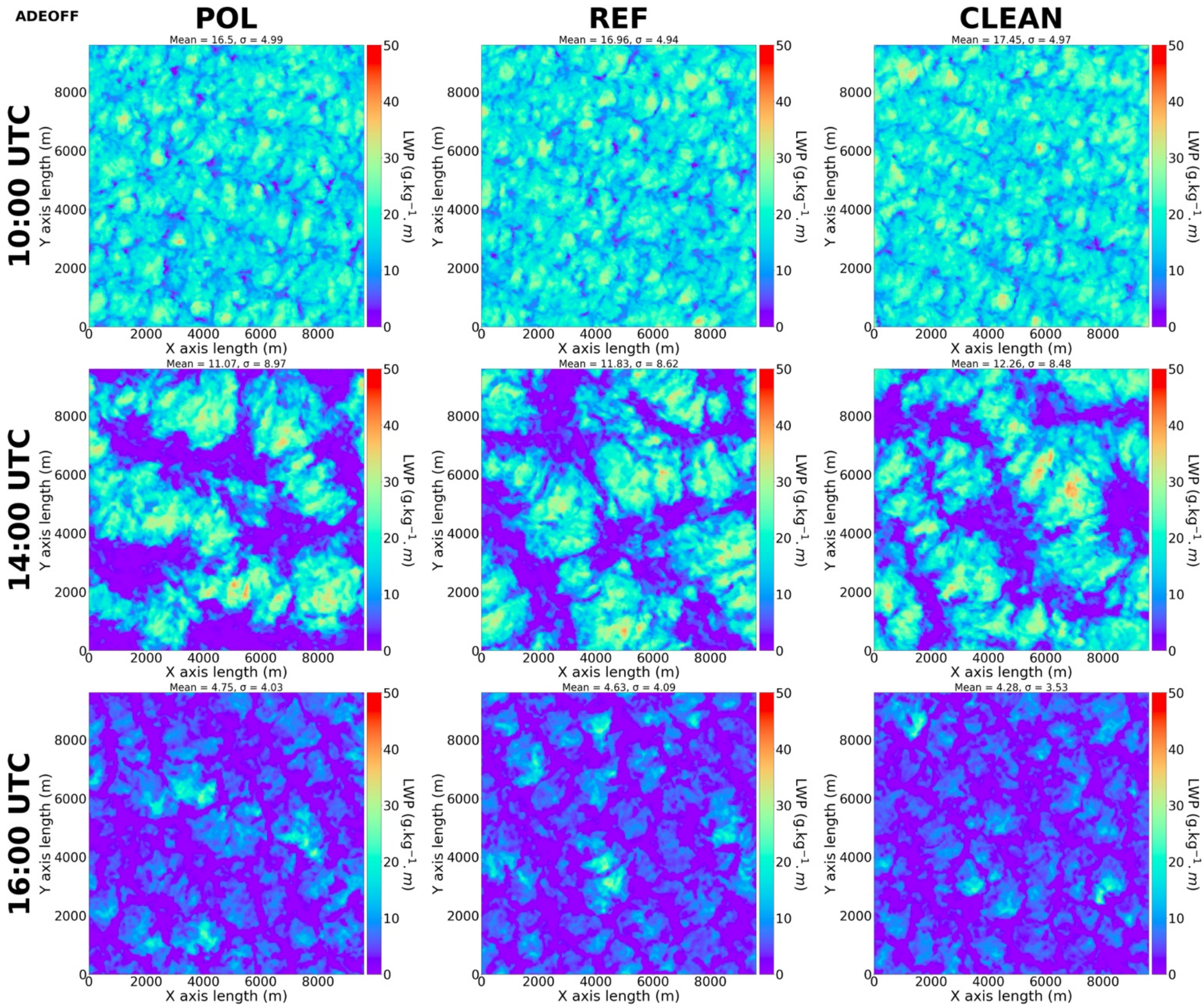

Figure A3. Liquid water path (LWP, *g kg*$^{-1}$ *m*) in POL (left column), REF (mid-column), and CLEAN (right column) ADEOFF runs at 10:00 UTC (top row), 14:00 UTC (middle row), and 16:00 UTC (bottom row).

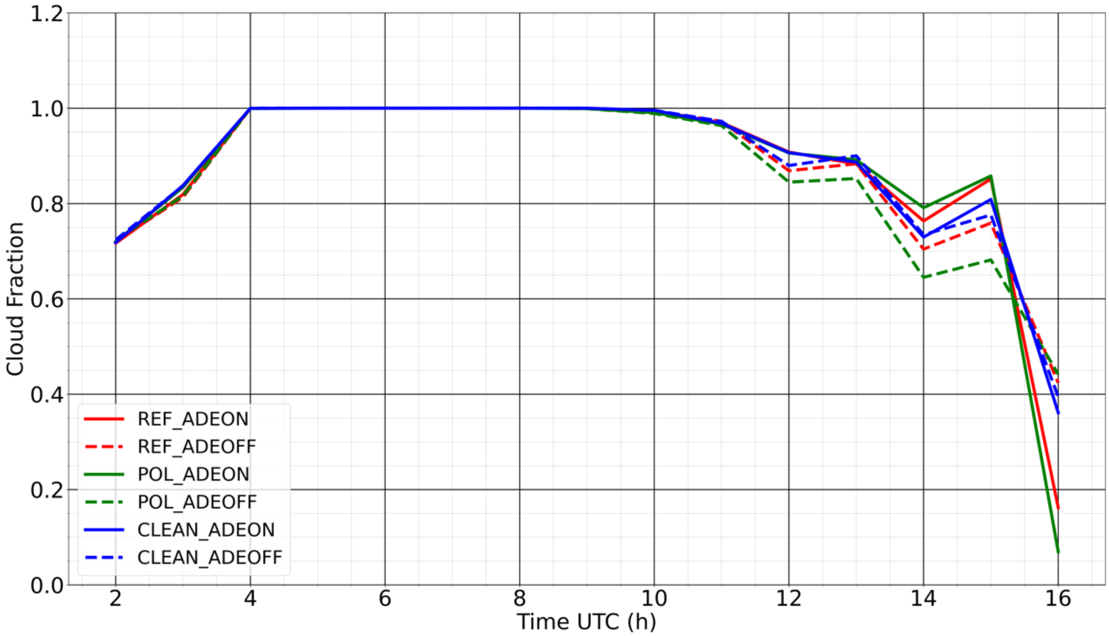

Figure A4. Domain averaged cloud fraction for AODON (solid lines) and AODOFF (dotted lines) of REF (red), POL (green), and CLEAN (blue) cases, derived using hourly model outputs. The cloud fraction here is a column quantity, defined as pixels where LWP > 5 *g kg^{-1} m*.

References

Abdul-Razzak, H. and Ghan, S. J.: A parameterization of aerosol activation: 2. Multiple aerosol types, *J. Geophys. Res.-Atmos.*, 105, 6837–6844, https://doi.org/https://doi.org/10.1029/1999JD901161, 2000.

Abdul-Razzak, H. and Ghan, S. J.: Parameterization of the influence of organic surfactants on aerosol activation, *J. Geophys. Res.-Atmos.,* 109, https://doi.org/https://doi.org/10.1029/2003JD004043, 2004.

Ackerman, A. S., Kirkpatrick, M. P., Stevens, D. E., and Toon, O. B.: The impact of humidity above stratiform clouds on indirect aerosol climate forcing, *Nature*, 432, 1014–1017, https://doi.org/10.1038/nature03174, 2004.

Adler, B., Babic, K., Kalthoff, N., Lohou, F., Lothon, M., Dione, C., Pedruzo-Bagazgoitia, X., and Andersen, H.: Nocturnal low-level´ clouds in the atmospheric boundary layer over southern West Africa: an observation-based analysis of conditions and processes, *Atmos. Chem. Phys.*, 19, 663–681, https://doi.org/10.5194/acp-19-663-2019, 2019.

Aouizerats, B., Thouron, O., Tulet, P., Mallet, M., Gomes, L., and Henzing, J. S.: Development of an online radiative module for the computation of aerosol optical properties in 3-D atmospheric models: validation during the EUCAARI campaign, *Geoscientific Model Development*, 3, 553–564, https://doi.org/10.5194/gmd-3-553-2010, 2010.

Babic, K., Adler, B., Kalthoff, N., Andersen, H., Dione, C., Lohou, F., Lothon, M., and Pedruzo-Bagazgoitia, X.: The observed diurnal cycle of low-level stratus clouds over southern West Africa: a case study, *Atmos. Chem. Phys.*, 19, 1281–1299, https://doi.org/10.5194/acp-19-1281-2019, 2019.

Bauer, S. E., Im, U., Mezuman, K., and Gao, C. Y.: Desert Dust, Industrialization, and Agricultural Fires: Health Impacts of Outdoor Air Pollution in Africa, *J. Geophys. Res.-Atmos.*, 124, 4104–4120, https://doi.org/https://doi.org/10.1029/2018JD029336, 2019.

Bellon, G. and Stevens, B.: Time Scales of the Trade Wind Boundary Layer Adjustment, *J. Atmos. Sci.*, 70, 1071 – 1083, https://doi.org/10.1175/JAS-D-12-0219.1, 2013.

Boucher, O., D. Randall, P. Artaxo, C. Bretherton, G. Feingold, P. Forster, V.-M. Kerminen, Y. Kondo, H. Liao, U. Lohmann, P. Rasch, S.K. Satheesh, S. Sherwood, B. Stevens, and X.Y. Zhang: Clouds and Aerosols. In: Climate Change 2013: The Physical Science Basis. Contribution of Working Group I to the Fifth Assessment Report of the Intergovernmental Panel on Climate Change [Stocker, T.F., D. Qin, G.-K. Plattner, M. Tignor, S.K. Allen, J. Boschung, A. Nauels, Y. Xia, V. Bex and P.M. Midgley (eds.)]. Cambridge University Press, Cambridge, United Kingdom and New York, NY, USA, 2013.

Bretherton, C. S., Blossy, F. N., and Uchida, J. : Cloud droplet sedimentation, entrainment efficiency, and subtropical stratocumulus albedo, *Geophys. Res. Lett*., 34, L03813, doi:10.1029/2006GL027648, 2007.

Brito, J., Freney, E., Dominutti, P., Borbon, A., Haslett, S. L., Batenburg, A. M., Colomb, A., Dupuy, R., Denjean, C., Burnet, F., Bourriane, T., Deroubaix, A., Sellegri, K., Borrmann, S., Coe, H., Flamant, C., Knippertz, P., and Schwarzenboeck, A.: Assessing the role of anthropogenic and biogenic sources on PM_1 over southern West Africa using aircraft measurements, *Atmos. Chem. Phys.*, 18, 757–772, https://doi.org/10.5194/acp-18-757-2018, 2018.

Caniaux, G., Redelsperger, J.-L., and Lafore, J.-P.: A Numerical Study of the Stratiform Region of a Fast-Moving Squall Line. Part I: General Description and Water and Heat Budgets, *J. Atmos. Sci.*, 51, 2046 – 2074, https://doi.org/10.1175/15200469(1994)051<2046:ANSOTS>2.0.CO;2,1994.

Carslaw, K. S., Gordon, H., Hamilton, D. S., Johnson, J. S., Regayre, L. A., Yoshioka, M., and Pringle, K. J.: Aerosols in the Pre-industrial Atmosphere, *Current Climate Change Reports*, 3, 1–15, https://doi.org/10.1007/s40641-017-0061-2, 2017.

Chatfield, R. B., Vastano, J. A., Li, L., Sachse, G. W., and Connors, V. S.: The Great African Plume from biomass burning: Generalizations from a three-dimensional study of TRACE A carbon monoxide, *J. Geophys. Res.-Atmos.*, 103, 28059–28077, https://doi.org/https://doi.org/10.1029/97JD03363, 1998.

Chen, T., Rossow, W. B., and Zhang, Y.: Radiative Effects of Cloud-Type Variations, *J. Clim*., 13, 264 – 286, https://doi.org/10.1175/1520-0442(2000)013<0264:REOCTV>2.0.CO;2, 2000.

Cleveland, W. S.: Robust Locally Weighted Regression and Smoothing Scatterplots, *Journal of the American Statistical Association,* 74, 829–836, https://doi.org/10.1080/01621459.1979.10481038, 1979.

Cohard, J.-M. and Pinty, J.-P.: A comprehensive two-moment warm microphysical bulk scheme. I: Description and tests, *Quar. J. Roy. Meteorol. Soc*., 126, 1815–1842, https://doi.org/https://doi.org/10.1002/qj.49712656613, 2000.

Dearden, C., Hill, A., Coe, H., and Choularton, T.: The role of droplet sedimentation in the evolution of low-level clouds over southern West Africa, *Atmos. Chem. Phys.*,18, 14253–14269, https://doi.org/10.5194/acp-18-14253-2018, 2018.

Deetz, K., Vogel, H., Knippertz, P., Adler, B., Taylor, J., Coe, H., Bower, K., Haslett, S., Flynn, M., Dorsey, J., Crawford, I., Kottmeier, C., and Vogel, B.: Numerical simulations of aerosol radiative effects and their impact on clouds and atmospheric dynamics over southern West Africa, *Atmos. Chem. Phys.*, 18, 9767–9788, https://doi.org/10.5194/acp-18-9767-2018, 2018.

Denjean, C., Bourrianne, T., Burnet, F., Mallet, M., Maury, N., Colomb, A., Dominutti, P., Brito, J., Dupuy, R., Sellegri, K., Schwarzenboeck, A., Flamant, C., and Knippertz, P.: Overview of aerosol optical properties over southern West Africa from DACCIWA aircraft measurements, *Atmos. Chem. Phys.*, 20, 4735–4756, https://doi.org/10.5194/acp-20-4735-2020, 2020a.

Denjean, C., Brito, J., Libois, Q., Mallet, M., Bourrianne, T., Burnet, F., Dupuy, R., Flamant, C., and Knippertz, P.: Unexpected Biomass Burning Aerosol Absorption Enhancement Explained by Black Carbon Mixing State, *Geophys. Res. Lett*., 47, e2020GL089055, https://doi.org/https://doi.org/10.1029/2020GL089055, e2020GL089055 2020GL089055, 2020b.

Deroubaix, A., Menut, L., Flamant, C., Brito, J., Denjean, C., Dreiling, V., Fink, A., Jambert, C., Kalthoff, N., Knippertz, P., Ladkin, R., Mailler, S., Maranan, M., Pacifico, F., Piguet, B., Siour, G., and Turquety, S.: Diurnal cycle of coastal anthropogenic pollutant transport over southern West Africa during the DACCIWA campaign, *Atmos. Chem. Phys.*, 19, 473–497, https://doi.org/10.5194/acp-19-473-2019, 2019.

Deroubaix, A., Menut, L., Flamant, C., Knippertz, P., Fink, A. H., Batenburg, A., Brito, J., Denjean, C., Dione, C., Dupuy, R., Hahn, V., Kalthoff, N., Lohou, F., Schwarzenboeck, A., Siour, G., Tuccella, P., and Voigt, C.: Sensitivity of low-level clouds and precipitation to anthropogenic aerosol emission in southern West Africa: a DACCIWA case study, *Atmos. Chem. Phys.*, 22, 3251–3273, https://doi.org/10.5194/acp-22-3251-2022, 2022.

Derrien, S., Bezombes, Y., Bret, B., Gabella, O., Jarnot, C., Medina, P., Piques, E., Delon, C., Dione, C., Campistron, B., Durand, P., Jambert, C., Lohou, F., Lothon, M., Pacifico, F., and Meyerfeld, Y.: DACCIWA field campaign, Savè super-site, UPS instrumentation, 10.6096/DACCIWA.1618, 2016.

Dione, C., Lohou, F., Lothon, M., Adler, B., Babic, K., Kalthoff, N., Pedruzo-Bagazgoitia, X., Bezombes, Y., and Gabella, O.: Low-level´ stratiform clouds and dynamical features observed within the southern West African monsoon, *Atmos. Chem. Phys.*, 19, 8979–8997, https://doi.org/10.5194/acp-19-8979-2019, 2019.

Eastman, R. and Warren, S. G.: Diurnal Cycles of Cumulus, Cumulonimbus, Stratus, Stratocumulus, and Fog from Surface Observations over Land and Ocean, *J. Clim.*, 27, 2386 – 2404, https://doi.org/10.1175/JCLI-D-13-00352.1, 2014.

Feingold, G., Jiang, H. L., and Harrington, J. Y.: On smoke suppression of clouds in Amazonia, *Geophys. Res. Lett.*, 32, 804, doi: 10.1029/2004GL021369, 2005.

Flamant, C., Deroubaix, A., Chazette, P., Brito, J., Gaetani, M., Knippertz, P., Fink, A. H., de Coetlogon, G., Menut, L., Colomb, A., Denjean, C., Meynadier, R., Rosenberg, P., Dupuy, R., Dominutti, P., Duplissy, J., Bourrianne, T., Schwarzenboeck, A., Ramonet, M., and Totems, J.: Aerosol distribution in the northern Gulf of Guinea: local anthropogenic sources, long-range transport, and the role of coastal shallow circulations, *Atmos. Chem. Phys.*, 18, 12363–12389, https://doi.org/10.5194/acp-18-12363-2018, 2018.

Flossmann, A. I. and Wobrock, W.: Cloud Processing of Aerosol Particles in Marine Stratocumulus Clouds, *Atmosphere*, 10, https://doi.org/10.3390/atmos10090520, 2019.

Fouquart, Y. and Bonnel, B.: Computations of solar heating of the earth's atmosphere – A new parameterizatio, *Beitrage zur Physik der Atmosphare*, 53, 35-62, 1980.

Geoffroy, O., Brenguier, J.-L., and Sandu, I.: Relationship between drizzle rate, liquid water path and droplet concentration at the scale of a stratocumulus cloud system, *Atmos. Chem. Phys.*, 8, 4641–4654, https://doi.org/10.5194/acp-8-4641-2008, 2008.

Ghonima, M., ~~T.~~ Heus, T., ~~J. R.~~ Norris, J. R., and J. Kleissl, J. ~~2016~~: Factors controlling stratocumulus cloud lifetime over coastal land, *J. Atmos. Sci.*, 73, 2961-2983, 2016.

Griffin, R. J., Nguyen, K., Dabdub, D., and Seinfeld, J. H.: A Coupled Hydrophobic-Hydrophilic Model for Predicting Secondary Organic Aerosol Formation, *J. Atmos. Chem.*, 44, 171–190, https://doi.org/10.1023/A:1022436813699, 2003.

Hagan, H. D., Thompson, B., Palmo, J., and Ruszkowski, A.: py-smps, https://github.com/quant-aq/py-smps, 2022.
Handwerker, J., Scheer, S., and Gamer, T.: DACCIWA field campaign, Savè super-site, Cloud and precipitation, https://doi.org/10.6096/dacciwa.1686, 2016.

Hannak, L., Knippertz, P., Fink, A. H., Kniffka, A., and Pante, G.: Why Do Global Climate Models Struggle to Represent Low-Level Clouds in the West African Summer Monsoon?, *J. Clim.*, 30, 1665 – 1687, https://doi.org/10.1175/JCLI-D-16-0451.1, 2017.

Hansen, J., M. Sato, R. Ruedy, A. Lacis, and V. Oinas, Global warming in the twenty-first century: An alternative scenario. *PNAS,* 97, 9875-9880, 1998.

Hartmann, D. L., Ockert-Bell, M. E., and Michelsen, M. L.: The Effect of Cloud Type on Earth's Energy Balance: Global Analysis, *J. Clim.*, 5, 1281 – 1304, https://doi.org/10.1175/1520-0442(1992)005<1281:TEOCTO>2.0.CO;2, 1992.

Haslett, S. L., Taylor, J. W., Evans, M., Morris, E., Vogel, B., Dajuma, A., Brito, J., Batenburg, A. M., Borrmann, S., Schneider, J., Schulz, C., Denjean, C., Bourrianne, T., Knippertz, P., Dupuy, R., Schwarzenböck, A., Sauer, D., Flamant, C., Dorsey, J., Crawford, I., and Coe, H.: Remote biomass burning dominates southern West African air pollution during the monsoon, *Atmos. Chem. Phys.*, 19, 15217–15234, https://doi.org/10.5194/acp-19-15217-2019, 2019.

Haywood, J. and Boucher, O.: Estimates of the direct and indirect radiative forcing due to tropospheric aerosols: A review, *Rev. Geophys.*, 38, 513–543, https://doi.org/https://doi.org/10.1029/1999RG000078, 2000.

Hill, P. G., Allan, R. P., Chiu, J. C., Bodas-Salcedo, A., and Knippertz, P.: Quantifying the Contribution of Different Cloud Types to the Radiation Budget in Southern West Africa, *J. Clim.*, 31, 5273 – 5291, https://doi.org/10.1175/JCLI-D-17-0586.1, 2018.

Huang, J., Wang, T., Wang, W., Li, Z., and Yan, H.: Climate effects of dust aerosols over East Asian arid and semiarid regions, *J. Geophys Res.-Atmos*, 119, 11,398–11,416, https://doi.org/https://doi.org/10.1002/2014JD021796, 2014.

Jiang, G.-S. and Shu, C.-W.: Efficient Implementation of Weighted ENO Schemes, *J. Comp. Phys.*, 126, 202–228, https://doi.org/https://doi.org/10.1006/jcph.1996.0130, 1996.

Jiang, H., Cotton, W. R., and Feingold, G.: Simulations of aerosol-cloud-dynamical feedbacks resulting from entrainment of aerosol into the marine boundary layer during the Atlantic Stratocumulus Transition Experiment, *J. Geophys. Res.*, 107, 4813, doi:10.1029/2001JD001502, 2002.

Jiang, H., and Feingold, G.: Effect of aerosol on warm convective clouds: Aerosol-cloud-surface flux feedbacks in a new coupled large eddy model, *J. Geophys. Res.*, 111, doi:10.1029/2005JD006138, 2006.

Johnson, B. T., Shine, K. P., and Forster, P. M.,: The semi-direct aerosol effect: Impact of absorbing aerosols on marine stratocumulus, *Q. J. R. Meteorol. Soc.*, 130, 1407-1422, 2004.

Kalthoff, N., Lohou, F., Brooks, B., Jegede, G., Adler, B., Babic, K., Dione, C., Ajao, A., Amekudzi, L. K., Aryee, J. N. A., Ay-´ oola, M., Bessardon, G., Danuor, S. K., Handwerker, J., Kohler, M., Lothon, M., Pedruzo-Bagazgoitia, X., Smith, V., Sunmonu, L., Wieser, A., Fink, A. H., and Knippertz, P.: An overview of the diurnal cycle of the atmospheric boundary layer during the West African monsoon season: results from the 2016 observational campaign, *Atmos. Chem. Phys.*, 18, 2913–2928, https://doi.org/10.5194/acp-18-2913-2018, 2018.

Khairoutdinov, M. and Kogan, Y.: A New Cloud Physics Parameterization in a Large-Eddy Simulation Model of Marine Stratocumulus, *Mon. Weather Rev.*, 128, 229 – 243, https://doi.org/10.1175/1520-0493(2000)128<0229:ANCPPI>2.0.CO;2, 2000.

Knippertz, P., Fink, A. H., Schuster, R., Trentmann, J., Schrage, J. M., and Yorke, C.: Ultra-low clouds over the southern West African monsoon region, *Geophys. Res. Lett.*, 38, https://doi.org/https://doi.org/10.1029/2011GL049278, 2011.

Knippertz, P., Coe, H., Chiu, J. C., Evans, M. J., Fink, A. H., Kalthoff, N., Liousse, C., Mari, C., Allan, R. P., Brooks, B., Danour, S., Flamant, C., Jegede, O. O., Lohou, F., and Marsham, J. H.: The DACCIWA Project: Dynamics–Aerosol–Chemistry–Cloud Interactions in West Africa, *Bull. Amer. Meteor. Soc.*, 96, 1451 – 1460, https://doi.org/10.1175/BAMS-D-14-00108.1, 2015.

Knippertz, P., Fink, A. H., Deroubaix, A., Morris, E., Tocquer, F., Evans, M. J., Flamant, C., Gaetani, M., Lavaysse, C., Mari, C., Marsham, J. H., Meynadier, R., Affo-Dogo, A., Bahaga, T., Brosse, F., Deetz, K., Guebsi, R., Latifou, I., Maranan, M., Rosenberg, P. D., and Schlueter, A.: A meteorological and chemical overview of the DACCIWA field campaign in West Africa in June–July 2016, *Atmos. Chem. Phys.*, 17, 10893–10918, https://doi.org/10.5194/acp-17-10893-2017, 2017.

Koch, D. and Del Genio, A. D.: Black carbon semi-direct effects on cloud cover: review and synthesis, *Atmos. Chem. Phys.*, 10, 7685–7696, https://doi.org/10.5194/acp-10-7685-2010, 2010a.

Koch, D. and Del Genio, A. D.: Black carbon semi-direct effects on cloud cover: review and synthesis, *Atmos. Chem. Phys.*, 10, 7685–7696, https://doi.org/10.5194/acp-10-7685-2010, 2010b.

Kreidenweis, S. M., Petters, M., and Lohmann, U.: 100 Years of Progress in Cloud Physics, Aerosols, and Aerosol Chemistry Research, *Meteorological Monographs*, 59, 11.1 – 11.72, https://doi.org/10.1175/AMSMONOGRAPHS-D-18-0024.1, 2019.

Lac, C., Chaboureau, J.-P., Masson, V., Pinty, J.-P., Tulet, P., Escobar, J., Leriche, M., Barthe, C., Aouizerats, B., Augros, C., Aumond, P., Auguste, F., Bechtold, P., Berthet, S., Bielli, S., Bosseur, F., Caumont, O., Cohard, J.-M., Colin, J., Couvreux, F., Cuxart, J., Delautier, G., Dauhut, T., Ducrocq, V., Filippi, J.-B., Gazen, D., Geoffroy, O., Gheusi, F., Honnert, R., Lafore, J.-P., Lebeaupin Brossier, C., Libois, Q., Lunet, T., Mari, C., Maric, T., Mascart, P., Mogé, M., Molinié, G., Nuissier, O., Pantillon, F., Peyrillé, P., Pergaud, J., Perraud, E., Pianezze, J., Redelsperger, J.-L., Ricard, D., Richard, E., Riette, S., Rodier, Q., Schoetter, R., Seyfried, L., Stein, J., Suhre, K., Taufour, M., Thouron, O., Turner, S., Verrelle, A., Vié, B., Visentin, F., Vionnet, V., and Wautelet, P.: Overview of the Meso-NH model version5.4 and its applications, *Geoscientific Model Development*, 11, 1929–1969, https://doi.org/10.5194/gmd-11-1929-2018, 2018.

Lunet, T., Lac, C., Auguste, F., Visentin, F., Masson, V., and Escobar, J.: Combination of WENO and Explicit Runge- Kutta methods for wind transport in Meso-NH model, *Mon. Weather Rev.*, 145, 3817–3838, https://doi.org/10.1175/MWR-D616-0343.12017, 2017.

Lascaux, F., Richard, E., and Pinty, J.-P.: Numerical simulations of three different MAP IOPs and the associated microphysical processes, *Quart. J. Roy. Meteorol. Soc.*, 132, 1907–1926, https://doi.org/https://doi.org/10.1256/qj.05.197, 2006.

Legain, D., Bousquet, O., Douffet, T., Tzanos, D., Moulin, E., Barrie, J., and Renard, J.-B.: High-frequency boundary layer profiling with reusable radiosondes, *Atmospheric Measurement Techniques*, 6, 2195–2205, https://doi.org/10.5194/amt-6-2195-2013, 2013.

Li, J., Carlson, B. E., Yung, Y. L., Lv, D., Hansen, J., Penner, J. E., Liao, H., Ramaswamy, V., Kahn, R. A., Zhang, P., Dubovik, O., Ding, A., Lacis, A. A., Zhang, L., and Dong, Y.: Scattering and absorbing aerosols in the climate system, *Nature Reviews Earth & Environment*, 3, 363–379, https://doi.org/10.1038/s43017-022-00296-7, 2022.

Liousse, C., Assamoi, E., Criqui, P., Granier, C., and Rosset, R.: Explosive growth in African combustion emissions from 2005 to 2030, *Environ. Res. Lett.*, 9, 035003, https://doi.org/10.1088/1748-9326/9/3/035003, 2014.

Liu, Y., Jia, R., Dai, T., Xie, Y., and Shi, G.: A review of aerosol optical properties and radiative effects, *Journal of Meteorological Research*, 28, 1003–1028, https://doi.org/10.1007/s13351-014-4045-z, 2014.

Lohmann, U. and Feichter, J.: Can the direct and semi-direct aerosol effect compete with the indirect effect on a global scale?, *Geophys. Res. Lett.*, 28, 159–161, https://doi.org/https://doi.org/10.1029/2000GL012051, 2001.

Lohou, F., Kalthoff, N., Adler, B., Babic, K., Dione, C., Lothon, M., Pedruzo-Bagazgoitia, X., and Zouzoua, M.: Conceptual model´ of diurnal cycle of low-level stratiform clouds over southern West Africa, *Atmos. Chem. Phys.*, 20, 2263–2275, https://doi.org/10.5194/acp-20-2263-2020, 2020.

Mari, C., Evans, M. J., Palmer, P. I., Jacob, D. J., and Sachse, G. W.: Export of Asian pollution during two cold front episodes of the TRACE-P experiment, *J. Geophys. Res.-Atmos.*, 109, https://doi.org/https://doi.org/10.1029/2003JD004307, 2004.

Mari, C. H., Cailley, G., Corre, L., Saunois, M., Attié, J. L., Thouret, V., and Stohl, A.: Tracing biomass burning plumes from the Southern Hemisphere during the AMMA 2006 wet season experiment, *Atmos. Chem. Phys.*, 8, 3951–3961, https://doi.org/10.5194/acp-8-3951-2008, 2008.

Marticorena, B. and Bergametti, G.: Two-year simulations of seasonal and interannual changes of the Saharan dust emissions, *Geophys. Res. Lett.*, 23, 1921–1924, https://doi.org/https://doi.org/10.1029/96GL01432, 1996.

Martin, G. M., Johnson, D. W., and Spice, A.: The Measurement and Parameterization of Effective Radius of Droplets in Warm Stratocumulus Clouds, *J. Atmos. Sci.*, 51, 1823 – 1842, https://doi.org/10.1175/15200469(1994)051<1823:TMAPOE>2.0.CO;2, 1994.

Masson, V., Le Moigne, P., Martin, E., Faroux, S., Alias, A., Alkama, R., Belamari, S., Barbu, A., Boone, A., Bouyssel, F., Brousseau, P., Brun, E., Calvet, J.-C., Carrer, D., Decharme, B., Delire, C., Donier, S., Essaouini, K., Gibelin, A.-L., Giordani, H., Habets, F., Jidane, M., Kerdraon, G., Kourzeneva, E., Lafaysse, M., Lafont, S., Lebeaupin Brossier, C., Lemonsu, A., Mahfouf, J.-F., Marguinaud, P., Mokhtari, M., Morin, S., Pigeon, G., Salgado, R., Seity, Y., Taillefer, F., Tanguy, G., Tulet, P., Vincendon, B., Vionnet, V., and Voldoire, A.: The SURFEXv7.2 land and ocean surface platform for coupled or offline simulation of earth surface variables and fluxes, *Geoscientific Model Development*, 6, 929–960, https://doi.org/10.5194/gmd-6-929-2013, 2013.

Menut, L., Flamant, C., Turquety, S., Deroubaix, A., Chazette, P., and Meynadier, R.: Impact of biomass burning on pollutant surface concentrations in megacities of the Gulf of Guinea, *Atmos. Chem. Phys.*, 18, 2687–2707, https://doi.org/10.5194/acp18-2687-2018, 2018.

Menut, L., Tuccella, P., Flamant, C., Deroubaix, A., and Gaetani, M.: The role of aerosol–radiation–cloud interactions in linking anthropogenic pollution over southern west Africa and dust emission over the Sahara, *Atmos. Chem. Phys.*, 19, 14657–14676, https://doi.org/10.5194/acp-19-14657-2019, 2019.

Metzger, S., Dentener, F., Pandis, S., and Lelieveld, J.: Gas/aerosol partitioning: 1. A computationally efficient model, *J. Geophys. Res.-Atmos.*, 107, ACH 16–1–ACH 16–24, https://doi.org/https://doi.org/10.1029/2001JD001102, 2002.

Mlawer, E. J., Taubman, S. J., Brown, P. D., Iacono, M. J., and Clough, S. A.: Radiative transfer for inhomogeneous atmospheres: RRTM, a validated correlated-k model for the longwave, *J. Geophys. Res.-Atmos.*, 102, 16663–16682, https://doi.org/https://doi.org/10.1029/97JD00237, 1997.

Morcrette, J.-J.: The Surface Downward Longwave Radiation in the ECMWF Forecast System, *J. Clim.*, 15, 1875 – 1892, https://doi.org/10.1175/1520-0442(2002)015<1875:TSDLRI>2.0.CO;2, 2002.

Murphy, J. G., Oram, D. E., and Reeves, C. E.: Measurements of volatile organic compounds over West Africa, *Atmos. Chem. Phys.*, 10, 5281–5294, https://doi.org/10.5194/acp-10-5281-2010, 2010.

Noilhan, J. and Planton, S.: A Simple Parameterization of Land Surface Processes for Meteorological Models, *Mon. Weather Rev*., 117, 536 – 549, https://doi.org/10.1175/1520-0493(1989)117<0536:ASPOLS>2.0.CO;2, 1989.

Pedruzo-Bagazgoitia, X., de Roode, S. R., Adler, B., Babic, K., Dione, C., Kalthoff, N., Lohou, F., Lothon, M., and Vilà-Guerau de´ Arellano, J.: The diurnal stratocumulus-to-cumulus transition over land in southern West Africa, *Atmos. Chem. Phys.*, 20, 2735–2754, https://doi.org/10.5194/acp-20-2735-2020, 2020.

Pinty, J.-P. and Jabouille, P.: A mixed-phased cloud parameterization for use in a mesoscale non-hydrostatic model: simulations of a squall line and of orographic precipitation, *Proc. Conf. on Cloud Physics,* 217–220. 1998.

Pruppacher, H. R., Klett, J. D., and Wang, P. K.: Microphysics of Clouds and Precipitation, *Aerosol Science and Technology*, 28, 381–382, https://doi.org/10.1080/02786829808965531, 1998.

Reeves, C. E., Formenti, P., Afif, C., Ancellet, G., Attié, J.-L., Bechara, J., Borbon, A., Cairo, F., Coe, H., Crumeyrolle, S., Fierli, F., Flamant, C., Gomes, L., Hamburger, T., Jambert, C., Law, K. S., Mari, C., Jones, R. L., Matsuki, A., Mead, M. I., Methven, J., Mills, G. P., Minikin, A., Murphy, J. G., Nielsen, J. K., Oram, D. E., Parker, D. J., Richter, A., Schlager, H., Schwarzenboeck, A., and Thouret, V.: Chemical and aerosol characterisation of the troposphere over West Africa during the monsoon period as part of AMMA, *Atmos. Chem. Phys.*, 10, 7575–7601, https://doi.org/10.5194/acp-10-7575-2010, 2010.

Sandu, I., Brenguier, J.-L., Geoffroy, O., Thouron, O., and Masson, V.: Aerosol Impacts on the Diurnal Cycle of Marine Stratocumulus, J. *Atmos. Sci*., 65, 2705 – 2718, https://doi.org/10.1175/2008JAS2451.1, 2008.

Sauvage, B., Thouret, V., Cammas, J.-P., Gheusi, F., Athier, G., and Nédélec, P.: Tropospheric ozone over Equatorial Africa: regional aspects from the MOZAIC data, *Atmos. Chem. Phys.*, 5, 311–335, https://doi.org/10.5194/acp-5-311-2005, 2005.

Schrage, J. M. and Fink, A. H.: Nocturnal Continental Low-Level Stratus over Tropical West Africa: Observations and Possible Mechanisms Controlling Its Onset, *Mon. Weather Rev*., 140, 1794 – 1809, https://doi.org/10.1175/MWR-D-11-00172.1, 2012.

Schuster, R., Fink, A. H., and Knippertz, P.: Formation and maintenance of nocturnal low-level stratus over the Southern West African monsoon region during AMMA 2006, *J. Atmos. Sci*., 70, 2337 – 2355, https://doi.org/10.1175/JAS-D-120241.1, 2013.

Stevens, B., Cotton, W. R., Feingold, G., and Moeng, C.-H.: Large-eddy simulations of strongly precipitating, shallow, stratocumulus-topped boundary layers, *J. Atmos. Sci*., 55, 3616-3638, 1998.

Stevens, B., Moeng, C.-H., Ackerman, A. S., Bretherton, C. S., Chlond, A., de Roode, S., Edwards, J., Golaz, J.-C., Jiang, H., Khairoutdinov, M., Kirkpatrick, M. P., Lewellen, D. C., Lock, A., Müller, F., Stevens, D. E., Whelan, E., and Zhu, P.: Evaluation of large-eddy simulations via observations of nocturnal marine stratocumulus, *Mon. Weather Rev*., 133, 1443–1462, https://doi.org/10.1175/MWR2930.1, 2005.

Stjern, C. W., Samset, B. H., Myhre, G., Forster, P. M., Hodnebrog, , Andrews, T., Boucher, O., Faluvegi, G., Iversen, T., Kasoar, M., Kharin, V., Kirkevåg, A., Lamarque, J.-F., Olivié, D., Richardson, T., Shawki, D., Shindell, D., Smith, C. J., Takemura, T., and Voulgarakis, A.: Rapid adjustments cause weak surface temperature response to increased black carbon concentrations, *J. Geophys. Res.-Atmos.*, 122, 11,462–11,481, https://doi.org/https://doi.org/10.1002/2017JD027326, 2017.

Taylor, J. W., Haslett, S. L., Bower, K., Flynn, M., Crawford, I., Dorsey, J., Choularton, T., Connolly, P. J., Hahn, V., Voigt, C., Sauer, D., Dupuy, R., Brito, J., Schwarzenboeck, A., Bourriane, T., Denjean, C., Rosenberg, P., Flamant, C., Lee, J. D., Vaughan, A. R., Hill, P. G., Brooks, B., Catoire, V., Knippertz, P., and Coe, H.: Aerosol influences on low-level clouds in the West African monsoon, *Atmos. Chem. Phys.*, 19, 8503–8522, https://doi.org/10.5194/acp-19-8503-2019, 2019.

Thouron, O., Brenguier, J.-L., and Burnet, F.: Supersaturation calculation in large eddy simulation models for prediction of the droplet number concentration, *Geoscientific Model Development*, 5, 761–772, https://doi.org/10.5194/gmd-5-761-2012, 2012.

Tulet, P., Crassier, V., Solmon, F., Guedalia, D., and Rosset, R.: Description of the mesoscale nonhydrostatic chemistry model and application to a transboundary pollution episode between northern France and southern England, *J. Geophys. Res.-Atmos.*, 108, ACH 5–1–ACH 5–11, https://doi.org/https://doi.org/10.1029/2000JD000301, 2003.

Tulet, P., Crassier, V., Cousin, F., Suhre, K., and Rosset, R.: ORILAM, a three-moment lognormal aerosol scheme for mesoscale atmospheric model: Online coupling into the Meso-NH-C model and validation on the Escompte campaign, *J. Geophys. Res.-Atmos.*, 110, ~~https://doi.org/~~https://doi.org/10.1029/2004JD005716, 2005.

Tulet, P., Grini, A., Griffin, R. J., and Petitcol, S.: ORILAM-SOA: A computationally efficient model for predicting secondary organic aerosols in three-dimensional atmospheric models, *J. Geophys. Res.-Atmos.*, 111, ~~https://doi.org/~~https://doi.org/10.1029/2006JD007152, 2006.

Twohy, C. H., Anderson, J. R., Toohey, D. W., Andrejczuk, M., Adams, A., Lytle, M., George, R. C., Wood, R., Saide, P., Spak, S., Zuidema, P., and Leon, D.: Impacts of aerosol particles on the microphysical and radiative properties of stratocumulus clouds over the southeast Pacific Ocean, *Atmos. Chem. Phys.*, 13, 2541–2562, https://doi.org/10.5194/acp-13-2541-2013, 2013.

Twomey, S.: PRECIPITATION BY DIRECT INTERCEPTION OF CLOUD-WATER, *Weather*, 12, 120–122, https://doi.org/https://doi.org/10.1002/j.1477-8696.1957.tb00453.x, 1957.

Van der Dussen, J. J., de Roode, S. R., and Siebesma, A. P.: Factors controlling rapid stratocumulus cloud thinning, J. *Atmos. Sci.*, 71, 655-664, https://doi.org/10.1175/JAS-D-13-0114.1, 2014.

Vié, B., Pinty, J.-P., Berthet, S., and Leriche, M.: LIMA (v1.0): A quasi two-moment microphysical scheme driven by a multimodal population of cloud condensation and ice freezing nuclei, *Geoscientific Model Development*, 9, 567–586, https://doi.org/10.5194/gmd-9-567-2016, 2016.

Wang, S., Wang, Q., and Feingold, G.: Turbulence, Condensation, and Liquid Water Transport in Numerically Simulated Nonprecipitating Stratocumulus Clouds, J. *Atmos. Sci.*, 60, 262–278, https://doi.org/10.1175/1520-0469(2003)060<0262:TCALWT>2.0.CO;2, 2003.

Wood, R.: Stratocumulus Clouds, *Mon. Weather Rev.*, 140, 2373 – 2423, https://doi.org/10.1175/MWR-D-11-00121.1, 2012.

Yamaguchi, T., Feingold, G., Kazil, J., and McComiskey, A.: Stratocumulus to cumulus transition in the presence of elevated smoke layers, *Geophys. Res. Lett.*, 42, 10,478–10,485, https://doi.org/https://doi.org/10.1002/2015GL066544, 2015.

Zhang, J. and Zuidema, P.: The diurnal cycle of the smoky marine boundary layer observed during August in the remote southeast Atlantic, *Atmos. Chem. Phys.*, 19, 14493–14516, https://doi.org/10.5194/acp-19-14493-2019, 2019.

Zouzoua, M., Lohou, F., Assamoi, P., Lothon, M., Yoboue, V., Dione, C., Kalthoff, N., Adler, B., Babic, K., Pedruzo-Bagazgoitia, X.,´ and Derrien, S.: Breakup of nocturnal low-level stratiform clouds during the southern West African monsoon season, *Atmos. Chem. Phys.*, 21, 2027–2051, https://doi.org/10.5194/acp-21-2027-2021, 2021.